

XSGRB - The X-shooter GRB afterglow sample

J. Selsing¹, T. Krühler¹, P. Goldoni¹⁴, D. Malesani¹, J. P. U. Fynbo¹, A. de Ugarte Postigo¹¹, J. Japelj²⁰, P. D’Avanzo,
Z. Cano, S. Covino¹⁰, V. D’Elia^{7, 12}, H. Flores, O. E. Hartoog⁶, J. Hjorth¹, P. Jakobsson⁵, A. Levan, A. Melandri,
S. Piranomonte⁷, R. Sánchez-Ramírez¹¹, S. Schulze^{17, 18}, N. R. Tanvir¹⁹, C. Thöne, S. D. Vergani^{7, 8}, P. M. Vreeswijk³,
D. J. Watson¹, K. Wiersema¹⁹, D. Xu¹, L. Christensen¹, A. De Cia³, L. Kaper⁶, L. A. Antonelli, F. Fiore, A. Gomboc,
P. Groot, F. Hammer, C. Ledoux², E. Maiorano, B. Milvang-Jensen¹, E. Palazzi, E. Pian, J. Schaye, G. Tagliaferri⁷,
R. A. M. J. Wijers⁶

¹ Dark Cosmology Centre, Niels Bohr Institute, University of Copenhagen, Juliane Maries Vej 30, 2100 København Ø, Denmark

² European Southern Observatory, Alonso de Córdova 3107, Vitacura, Casilla 19001, Santiago 19, Chile

³ Department of Particle Physics and Astrophysics, Faculty of Physics, Weizmann Institute of Science, Rehovot 76100, Israel

⁴ Thüringer Landessternwarte Tautenburg, Sternwarte 5, 07778 Tautenburg, Germany

⁵ Centre for Astrophysics and Cosmology, Science Institute, University of Iceland, Dunhagi 5, IS-107 Reykjavik, Iceland

⁶ Astronomical Institute Anton Pannekoek, University of Amsterdam, Science Park 904, NL-1098 XH Amsterdam, the Netherlands

⁷ INAF-Osservatorio Astronomico di Roma, Via Frascati 33, I-00040 Monteporzio Catone, Italy

⁸ GEPI-Observatoire de Paris, CNRS UMR 8111, Univ. Paris-Diderot, 5 Place Jules Janssen - 92190 Meudon, France

⁹ American River College, Physics and Astronomy Dpt., 4700 College Oak Drive, Sacramento, CA 95841, USA

¹⁰ INAF, Osservatorio Astronomico di Brera, Via E. Bianchi 46, I-23807 Merate, Italy

¹¹ Instituto de Astrofísica de Andalucía (IAA-CSIC), Glorieta de la Astronomía s/n, 18008, Granada, Spain

¹² ASI-Science Data Centre, Via Galileo Galilei, I-00044 Frascati, Italy

¹³ Institute of Experimental and Applied Physics, Czech Technical University in Prague, Horska 3a/22, 128 00 Prague 2, Czech Republic

¹⁴ APC, Astroparticules et Cosmologie, Université Paris Diderot, CNRS/ IN2P3, CEA/Irfu, Observatoire de Paris, Sorbonne Paris Cité, 10, Rue Alice Domon et Léonie Duquet, 75205 Paris Cedex 13, France

¹⁵ Max-Planck-Institut für extraterrestrische Physik, Giessenbachstraße, 85748 Garching, Germany

¹⁶ Università degli studi di Milano-Bicocca, Piazza della Scienza 3, 20126, Milano, Italy

¹⁷ Pontificia Universidad Católica de Chile, Departamento de Astronomía y Astrofísica, Casilla 306, Santiago 22, Chile

¹⁸ Millennium Center for Supernova Science

¹⁹ Department of Physics and Astronomy, University of Leicester, University Road, Leicester, LE1 7RH, UK

²⁰ University of Ljubljana, Department of Physics, Faculty of Mathematics & Physics, SI

Received/ accepted

ABSTRACT

The *Swift* satellite allows us to use gamma-ray bursts (GRBs) to peer into the hearts of star forming galaxies through cosmic time. Our open collaboration, representing most of the active ESO member researchers in this field, seeks to build a public legacy sample of GRB X-shooter spectroscopy while *Swift* continues to fly. We propose to continue our programme to target all suitably observable GRB afterglows (up to 15 bursts per semester), with the primary goal of producing a well-defined, homogeneous, statistically useful sample. To date, our spectroscopy covers a redshift range from 0.059 to about 8, with more than 20 robust metallicity measurements from absorption lines (over the redshift range 1.7–5.9) and 4 secure detections of H₂ or CH molecular absorption. Such information is extremely difficult to obtain by other means. In terms of studying the spread and redshift evolution in gas-phase properties, the sample is still limited by low-number statistics.

Key words. Gamma-ray burst: individual: GRB 120815A — galaxies: high-redshift — ISM: molecules — dust, extinction

1. Introduction

Gamma-Ray bursts (GRBs) are interesting as they provide the opportunity to derive new insights into a very wide range of topics in astrophysics. Examples range from small scale phenomena relating to the magnetars, properties of highly relativistic jets, hyper/supernova explosions, the interstellar medium, dust extinction curves, starburst galaxies, chemical and molecular abundances, escape of ionizing radiation, the ionization state of the

intergalactic medium, intervening absorption systems to standard candles in cosmology. In that sense GRB research is very multi-disciplinary.

The *Swift* satellite (?), which was launched in 2004, has made it possible to harvest much of the great potential in using GRBs as probes of galaxies in the intergalactic medium, which was already hinted at by results from earlier missions (e.g. ?). A crucial aspect of the great success of the *Swift* mission has been the extensive ground based follow-up observations of the afterglows and of the host galaxies of the GRBs. This work has involved a large community of researchers both inside and outside the official *Swift* team. This fruitful collaboration has been

* Based on observations collected at the European Southern Observatory, Paranal, Chile, Program ID: 098.A-0055, 097.A-0036, 096.A-0079, 095.B-0811(B), 095.A-0045, 094.A-0134, 093.A-0069, 092.A-0124, 0091.C-0934, 090.A-0088, 089.A-0067, 088.A-0051, 087.A-0055, 086.A-0073, 085.A-0009 and 084.A-0260

greatly facilitated by the open data access policy of the *Swift* mission.

In the beginning of the "*Swift* era" most of the follow-up spectroscopy was secured using low-resolution spectrographs (typically $R=\lambda/\Delta\lambda < 1000$, e.g. Fynbo et al. 2009). Low-resolution spectroscopy is powerful for a number of reasons, first of all is the ability to secure information for even very faint targets. This allows the measurements of a number of important parameters such as redshifts, spectral slopes, and extinction. For a handful of very bright afterglows high-resolution (typically $R > 20000$) spectra were secured and for these events much more information about conditions inside the host galaxies were extracted (e.g., ???).

The X-shooter spectrograph (Vernet et al. 2011) is the first of the 2nd generation instruments at the ESO Very Large Telescope (VLT). It is a high-throughput echelle spectrograph covering the full spectra range from the UV atmospheric cutoff around 300 nm to the near-infrared (near-IR) K-band ending around 2500 nm with three spectral arms (UVB, VIS, NIR). It was designed very much with transient source follow-up in mind as the fading luminosities of such sources makes it urgent to secure as extensive coverage as possible in the shortest possible time. At the same time the resolution was set to be in the range 4000–9000 in order to be able to get a large useful spectra range between the many sky-background emission lines in the red and near-IR spectral ranges. In this paper we present the results of a dedicated effort over the years 2009 – 2016 to use the X-shooter spectrograph to secure spectroscopic observations of afterglows and host galaxies of GRBs detected by *Swift*. All data resulting from the survey are publicly available in reduced form.

The paper is organized in the following way: In Sect. 2 we describe the sample including the sample selection criteria and the observational strategy. In Sect. 4 we describe the results of the survey, i.e. the efficiency of the follow-up effort and the characteristics of the observed bursts. We also here assess the completeness of the finally realized sample. Finally, we offer our conclusions in Sect. 5.

2. Sample selection criteria and observations

2.1. Sample selection criteria

Being of transient nature, it is difficult to impose strong sample selection criteria on GRBs, without hampering the follow-up effort. Many natural follow-up restrictions exist from already, being it weather conditions, pointing restrictions of the telescope or poorly localized bursts as reported by the *Swift*-telescope. To maximize the return of the follow-up campaign we have chosen a few selection criteria that attempts to provide an unbiased selection of bursts, while allowing for a high success-rate

1. GRB triggered onboard by *Swift*.
2. Galactic $A_V \lesssim 0.5$ mag.
3. XRT started observing within 10 minutes since the GRB; an XRT position must be distributed within 12 hr.
4. The target must be visible for at least 60 minutes at least 30 degrees above the horizon, with the Sun below -12.
5. No bright closeby stars.

¹ Note that in the P84 proposal the criteria have been stated a bit differently, the visibility constraint being replaced by a declination + Sun angle constraint. The above criteria are however those defining the sample.

A significant fraction of the bursts presented here (Insert exact number) have already had their hosts investigated in Krühler et al. (2015), for which extractions of the hosts exist. The focus of the data presented here are on the afterglows themselves and in the absence of a clear afterglow, the host. We will not, however, investigate the hosts.

We simultaneously want to minimize any biases against astrophysical conditions while at the same time maximizing likelihood of observations. By restricting the selection criteria to conditions local to Galaxy.

2.2. Follow-up procedure

2.2.1. RRM observations

The rapid-response mode is

2.3. Observations

All the observations in this sample has been carried out using the cross-dispersed echelle spectrograph, X-shooter (Vernet et al. 2011), mounted on two of the four Unit Telescopes at ESO/VLT, UT2 (Kueyen) and UT3 (Melipal) during the duration of this follow-up campaign, which covers the entire lifetime of X-shooter. Observations have been carried out from the ESO period P84 through P98 under the following programme IDs: 098.A-0055, 097.A-0036, 096.A-0079, 095.A-0045, 094.A-0134, 093.A-0069, 092.A-0124, 0091.C-0934, 090.A-0088, 089.A-0067, 088.A-0051, 087.A-0055, 086.A-0073, 085.A-0009 and 084.A-0260.

The first GRB followed up is GRB090313, observed 15th of March 2009, which was while X-shooter was mounted on UT3 during the commissioning of the instrument. The bursts observed during the commissioning period is not a part of our statistical sample, but are nonetheless published as part of the bursts observed by the X-shooter GRB team. The first burst observed after science verification was completed when X-shooter was moved to UT2 is GRB091018 which thereby constitute the first burst entering our statistical sample. For all bursts that fulfill our sample selection criteria, described in Sect. 2.1, spectroscopic follow-up has been attempted with X-shooter. Various conditions can affect our ability to follow up a given burst, and a discussion of this effect is included in Sect. 4.3.

X-shooter can cover the spectral wavelength region from 300 nm to 2480 nm in a single exposure, by splitting the light in three separate spectroscopic arms using dichroics. This way each arm work as a separate instrument, each functioning as its own echelle spectrograph. The ultraviolet blue(UVB) arm covering 3000 - 550 nm, the visual(VIS) arm covering 550 - 1020 nm, and the near-infrared(NIR) arm covering 10200 - 2480 nm with the possibility of applying a k-band blocking filter cutting the coverage of the NIR arm at 1020 - 2100 nm.

(ABBA)

For the large majority of the bursts we have observed with a slit width of 1''.0, 0''.9, and 0''.9 for the UVB, VIS, and NIR-arm respectively, which puts a lower limit on the delivered resolution of the spectra based on the tabulated values of the delivered resolutions, which is 4350, 7450, and 5300 for the UVB, VIS and NIR-arm respectively². The slit width also sets the width of the atmospheric sky lines and determines the amount of light lost

² <https://www.eso.org/sci/facilities/paranal/instruments/xshooter/inst.html>

due to the wavelength-dependent seeing PSF extending outside the coverage of the slit, where the width of sky-lines is always set by the slit width whereas both the delivered resolution and the slitloss changes for the better as the seeing PSF drops below the slit width. For atmospheric conditions delivering a seeing PSF with a FWHM of $0''.9$ observed with a $0''.9$ slit only 76.1 percent of the light will enter the slit, meaning that for almost all observations a slitloss correction is required. We describe how slitlosses were corrected for in Sect. 3.1. For accurate measurements of velocity widths, a precise instrumental resolution is required and this becomes better when the delivered seeing is better than the slit width. We discuss this in Sect. 3.5.

(ADC discussion)

We list the overview of all the observations in Tab. 1.

3. Data processing

In this section we describe how the final data products are produced and subsequently post-processed. All post-processing scripts developed for this dataset are made publicly available at https://github.com/jselsing/XSGRB_reduction_scripts, along with instructions of use.

Before any reductions are done, the raw object images are run through the cosmic-ray removal algorithm (van Dokkum 2001) implementation, *Astro-SCRAPPY*³, where a wide clipping radius have been used around detected cosmics to ensure that edge residuals are robustly rejected.

The basis for the reductions is the VLT/X-shooter pipeline, version 2.7.1 or newer (Goldoni et al. 2006; Modigliani et al. 2010). The pipeline is managed with the Reflex interface (Freudling et al. 2013) and is used for subtraction of bias level, flat-fielding, tracing of the echelle orders, wavelength calibrations with the use of arc-line lamps, flux calibration using spectrophotometric standards (Vernet et al. 2009; Hamuy et al. 1994), mirror flexure compensation, initial sky-subtraction and lastly the rectification and merging of the orders. For the initial sky-subtraction, the background has been estimated in regions adjacent to the object trace clear of contaminating sources. Because of the broken ADC, for some objects there is a lot of curvature in the object trace. This means that for some bursts, the initial sky-estimate has been made from a limited number of pixels in the spatial direction. By doing an initial subtracting the sky on the un-rectified image we ensure that bulk of the sky background is not redistributed by the rectification process.

The image is rectified onto an equidistant grid with a dispersion sampling of 0.02 nm/pixel and a 0.16 "/pixel spatial sampling for the UVB and VIS arm and 0.06 nm/pixel with a 0.21 "/pixel in the NIR arm. Because the tabulated resolution is a lower limit, by choosing a sampling of 0.02 nm/pixel, we ensure that the bluest part of neither of the arms have a sampling lower than the Nyquist sampling rate of 2 pixels per resolution FWHM.

3.1. Post-processing

For a typical observation, each of the exposures in the nodding sequence has been reduced as single observation and then subsequently combined to form a single image. Because this strategy is employed, we can reject outliers in the stack and weight by the average inverse variance of the background. When weighting images where the noise in each pixel is dominated by Poisson noise it important to estimate the background variance in a

large enough region, so that to remove the correlation between the signal and the weights. To this end, the weight map is generated by a running median window over the variance map, where the trace as been masked and width of the window is chosen to be wide enough for median variance to be generated on the basis of several hundred pixels. This weighting scheme automatically also optimally combines images of different exposure times or images where the background is varying, which is often the case when a burst has been observed close to twilight

Because the background is very bright and there is a high abundance of broad sky-lines in the NIR arm, when there are no contaminating sources in the slit, the sky has been put back on the images and they have been reduced in pairs of two, subtracting the two from each other, keeping the WCS static. This amounts to the regular nodding reduction, only we can reject outliers and weight by the averaged inverse variance map.

By STARE reducing all observations we additionally get a spectrum of the sky, which we can use to calibrate the wavelength solution in Sect. 3.2.

3.2. Correction for offsets in the wavelength calibration

X-shooter, being installed at the VLT Cassegrain focus is prone to flexures during operations. The flexures modify the projection of the slit on the detector with respect to the one obtained in day-time calibration. This requires a modification of the wavelength solution in order to process correctly the night-time data. Part of this correction is performed by the pipeline using the frames taken during X-shooter Active Flexure Compensation procedure⁴.

The remaining offset is corrected by cross-correlation with a synthetic sky spectrum (Noll et al. 2012; Jones et al. 2013) after the continuum, estimated as the mode of all flux values, has been subtracted. To get the correct seeing PSF with which to convolve the synthetic sky an initial refinement of the wavelength solution have been obtained by cross-correlating the observed sky with an unconvolved synthetic sky. This preliminary wavelength calibration is applied to the observed sky. The synthetic spectrum is then convolved with an increasing seeing PSF and the width that minimizes χ^2 with the updated observed sky is chosen to be the effective sky-PSF. Using the synthetic sky with the matched resolution, a final wavelength calibration can then be calculated by cross-correlating the observed sky with the correctly broadened sky spectrum, as a function of a velocity offset. Both a multiplicative and an additive offset to the wavelength calibration has been tested, but in terms of χ^2 , the model with only a multiplicative offset is preferred.

The resulting offsets, which were smaller than 0.01 nm in the UVB and VIS data and smaller than 0.05 nm in the NIR spectra, but changing over short period of time were applied to the corresponding spectra.

Using the convolved synthetic sky, the $\geq 3\sigma$ sky brightness pixels have been added to the bad pixel map to avoid the cores of the brightest sky-lines.

3.3. Spectral extraction

To extract the afterglow spectrum from the rectified 2D-image, several techniques have been employed based on the brightness of the afterglow and the complexity of the objects entering the slit. Due to the malfunctioning ADC, see Sect. 2.3, the spec-

³ <https://github.com/astropy/astroscrappy>

⁴ X-shooter User Manual available at <https://www.eso.org/sci/facilities/paranal/instruments/xshooter/doc.html>

tral trace moves across the slit as a function of wavelength for a large fraction of the bursts observed meaning that using a single aperture for the spectral extraction is inadequate due to the large amount of background that would then enter the slit. To optimally select the extraction regions we therefore need to model the trace position.

To get the shape and the position of the spectral PSF as a function of location on the image, we need to choose a model which can represent how the light falls on the slit. We know from Trujillo et al. (2001) that the Moffat function (Moffat 1969) adequately describes an imaging PSF due to atmospheric turbulence, but due to the aberrations in the dispersion elements and the rectification process, the PSF we are trying to model different from this profile. To allow for flexibility in the model, we have chosen the Voigt function as a model for the spectral PSF and we describe how this is evaluated in App. A. Since additionally, the host galaxy could also have a contribution the image profile, this choice allows for the required freedom if additional flux is in the wings of the profile.

To guide the guess position of the trace on the slit as a function of wavelength, we have used the analytic prescription for the trace position described in Filippenko (1982), where the header keywords of the observations have been queried for the ambient conditions which controls the degree to which the trace moves.

Based on the signal-to-noise of the afterglow continuum, the 2D-image has been binned down in the spectral direction to a number of elements that allows for an accurate tracing of the PSF, typically 200 bins for moderate signal-to-noise. For each of the bins and using the guess position, the spectral PSF has been fit using the unweighted chi-squared minimization algorithm implemented in `scipy.optimize.curve_fit` (Jones et al. 2001). Since we know that the trace varies slowly as a function of wavelength, we have then fitted a low-order polynomial to the fit parameters as a function of wavelength, which allows us to evaluate the spectral PSF at all wavelengths and this way accurately model the entire spectral PSF.

Equipped with a model for how the light falls on the entire image, we can then employ the optimal extraction algorithm Horne (1986), which weights the extraction aperture by the spectral profile, or alternatively sum all pixels within 1 FWHM of the modeled profile. Where possible, we have used the optimal extraction. In cases where the trace is very weak, even in the binned images, an aperture has been selected manually which covers emission lines, if present, and when nothing is immediately visible, the entire nodding window. The error- and bad pixel maps are in all cases propagated throughout the extraction.

In cases where multiple traces are visible in the slit, additional components for the profile are used in the optimal extraction. The additional components do not share the PSF parameters and in cases where the additional component is an extended object, the fits have been inspected to ensure that the additional component does not skew the fit towards a different PSF. The additional components are not used for the weights.

The spectra are corrected for galactic extinction using the $E(B-V)$ value from the dust maps of Schlegel et al. (1998) with the update in Schlafly & Finkbeiner (2011)⁵, and the extinction curve by Cardelli et al. (1989) with a total to selective extinction $R_V = 3.1$. The wavelengths of the extracted 1D-spectra are moved to vacuum, moved to the barycentric frame, and the wavelength recalibration described in Sect. 3.2 is applied. Pixels with

pixel-to-pixel variation large than 50σ are added to the bad pixel map.

3.4. Telluric correction

For all earth-based telescopes, the light of interest has to pass through Earth's atmosphere, where the atmospheric content and conditions make an imprint on the received spectrum. These telluric features can be calculated in a multitude of ways and we employ a prioritized list of methods here, depending on the availability of the different method. Since the observations are often taken at odd times under varying conditions, this prioritized list ensures that we are always doing the optimal correction.

The highest priority method is using the GRB afterglow continuum itself, where the atmospheric conditions have directly been imprinted on the spectrum. The telluric features can directly be fit with an atmospheric model (Smette et al. 2015; Kausch et al. 2015), which can then be used to correct for the absorption. The accuracy of the correction depends on the The requirement here is that the afterglow continuum spectrum has a signal-to-noise higher than a value of 10.

If the afterglow is not sufficiently bright, telluric standard stars observed close in the time to the GRB can be used as a proxy for the atmospheric condition during the GRB observation. Here we employ the telluric correction method that has been developed in Selsing et al. (2015), where a library of synthetic templates is fit to the observed telluric standard.

In the last case, where the object is neither bright enough, or there for some reason have not been observed a telluric standard, we rely on the synthetic sky model by (Noll et al. 2012; Jones et al. 2013) for which we generate a synthetic transmission spectrum, which we then use, where the ambient parameters for the observations have been used.

3.5. Spectral resolution

The afterglow spectra described in this paper are obtained in Target-of-Opportunity (override) mode. In most cases there is therefore little possibility to tweak slit widths to the seeing at the time of observations (i.e. to optimise spectral resolution and signal to noise), and almost all our data is therefore taken with a fixed set of slit widths and binning, described above. In a fair number of cases, the seeing full width at half maximum (FWHM) is considerably smaller than the slit width, and the delivered spectral resolution will then be determined by the seeing rather than slit width, as afterglows are point sources (this is evidently not the case for extended sources, e.g for host galaxies). The delivered resolution for slit width dominated spectra post-reduction and extraction can easily be determined from the bright sky emission lines. For afterglow spectra with very high signal to noise, the delivered spectral resolution can at times be determined from the science data themselves. However, in the presence of multiple velocity components in absorption, other forms of line broadening, and a lack of lines at some redshifts, this is difficult to do at poorer signal to noise ratios (the majority of spectra in our sample). A broad starting value for the expected resolution will help fitting of these spectra, and can be important in upper limit determination, and for this reason we construct a aim to construct a crude relation between the seeing and the delivered resolution at our slit width, binning, and reduction pipeline settings. To this end we use observations of telluric standard stars that are taken with identical instrument settings as our afterglow spectra, usually just after the science data, as

⁵ Queried from <http://irsa.ipac.caltech.edu/applications/DUST/index.html> using Ginsburg et al. (2016)

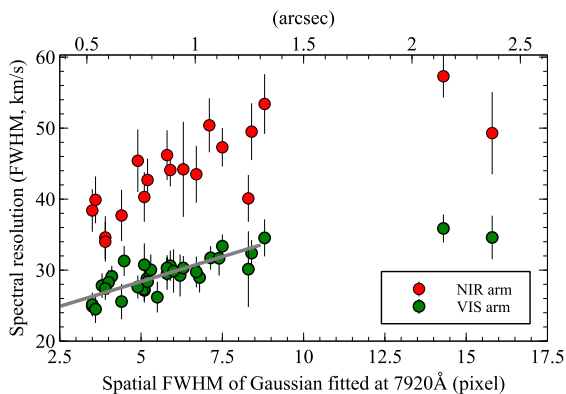


Fig. 1: Green datapoints show the FWHM (km/s) of Gaussian fits to unresolved telluric absorption lines in the VIS spectra, as a function of the FWHM of a Gaussian fit onto the trace in spatial direction at 792 nm. The lower horizontal axis is in units pixels, the top axis in arc seconds. The red datapoints show a subsample of NIR spectra. The grey line shows a linear fit to the VIS datapoints.

part of the ESO X-shooter calibration plan. These spectra have been reduced together with the afterglow spectra, using identical pipeline settings with the same version of the pipeline. First we fit a Gaussian function in the spatial direction of the trace of the standard star at 792 nm (i.e. in the VIS arm). After this, we fit a series of 20 telluric absorption lines in the telluric standard star spectra with Gaussians, taking care to select transitions that are not almost-resolved multiples, should be intrinsically unresolved, and are in areas with well defined continuum flux. We pick 34 telluric standard stars spanning a range of DIMM seeing values, with the majority between $0.5 - 1.5 \text{ arcsec}$. The resulting distribution of spectral FWHM (km/s) as a function of spatial FWHM at 792 nm is fairly well described by a linear relation $a + b * x$, with x the spatial FWHM in pixels (with 0.15 arc sec per pixel), $a = 21.4 \pm 1.3 \text{ km/s}$, $b = 1.4 \pm 0.2$. We use this linear relation as a way to estimate the spectral resolution for medium to poor signal to noise afterglow spectra in the VIS arm. To extend this to the UVB and NIR arm, we measured a series of lines in NIR arm spectra of a subset of 19 sources used for the VIS arm above, and find that the resulting distribution is consistent with a simple scaling of the VIS arm relation by the ratio of resolutions of the NIR and VIS arm for unresolved, slit filling, sources as given on the ESO instrument website. The UVB arm contains no suitable absorption lines to use, and we therefore use a scaled value as in the NIR arm. While this simple method is not terribly accurate (for one, the spatial profile of the trace is not a perfect Gaussian), but it gives a sufficiently accurate estimate for the analysis of these poor signal to noise science spectra.

4. Results

In this section we describe the efficiency of the follow-up effort and the characteristics of the observed bursts. We also assess the degree to which the sample obtained is complete.

4.1. Follow-up timing and afterglow brightness

A rapid follow-up is essential for the accurate designation of GRB the origin. The redshift determination of burst where the host is not easily

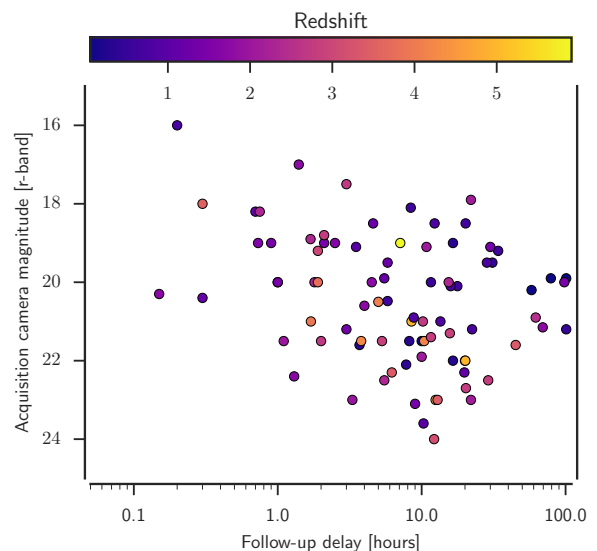


Fig. 2: Follow-up timing and afterglow magnitude at the start of observation. The points have been colored based on the redshift of the corresponding burst.

4.2. Sample completeness

Based on the sample criteria specified in Sect. 2.1, a total of 152 (Get number) bursts has been triggered by *Swift* in the period since the comissioning of VLT/X-shooter in (Get date). This constitutes the *statistical sample*.

4.3. Properties of rejected triggers

How many bursts have been excluded due to particularities in the follow-up attempt. Visitor, Weather, technical issues.

4.4. On the nature of triggered GRBs without detected optical afterglow.

This should include observations where the acquisition image has been taken, but observations were discontinued due to non-detection. What are the X-ray properties of these bursts?

4.5. Redshifts

4.5.1. Afterglow-based redshifts

4.5.2. Emissionline-based redshifts

Redshift completeness

4.6. Hydrogen column densities

Because the locations of GRBs are associated with the most intensely starforming regions (Hogg & Fruchter 1999; Bloom et al. 2002; Fruchter et al. 2006), the GRB afterglow light has to propagate through the large amounts of hydrogen fueling the star formation. Because a significant fraction of the hydrogen has not been ionized yet, the optical depth at the wavelength of $\text{Ly}\alpha$ is very high, saturating at the line center. This causes a strong absorption system to appear in the afterglow continuum. For bursts with $z \gtrsim 1.7$, the position of $\text{Ly}\alpha$ moves into the spectroscopic

coverage of X-shooter, meaning that we are able to detect this absorption trough due to Ly α .

Due of the stochastic nature of the Ly α -forest, the blue wing of the Lyman alpha absorption line is randomly superposed with forest systems, along with strong absorption from Mn II and Si III, making it notoriously difficult to model. Additionally, Similarly so, the red wing has got the ISM signatures imprinted on it, especially strong absorption due to Si II, [S II] and [N V] which can exhibit significant velocity structure. Along with instrumental effects, the generative model for the data that we would use in a likelihood-based analysis would be almost boundless in complexity, making formal fitting of the column densities outside the scope of this paper.

Using an analytic approximation to an absorption line profile and it's dependence on the column density (Tepper García 2006), we overplot a synthetic absorption line with a specified column density on our observed spectrum. By tuning the value of the hydrogen column density until the synthetic absorption line matches the spectrum, we can thereby infer the actual column density of the GRB sight line in a manual way. In a similar fashion, the errors on the hydrogen column can be inferred. We show the results of this procedure for all bursts where possible in Fig. 3 and the inferred hydrogen column densities in Tab. 2

5. Discussion and conclusions

In this paper we have presented the results of a dedicated effort over the years 2009 – 2016 to use the X-shooter spectrograph on the ESO-VLT to secure spectroscopic observations of afterglows and host galaxies of GRBs detected by *Swift*. This work was initiated by a consortium using Guaranteed Time on X-shooter, but over the years the project continued in open time and the team was opened to include any researchers interested in contribution to this effort.

The sample we present here include spectroscopic observations of 86 systems fulfilling our sample criteria of which 72 are afterglow spectra and 14 are observations of the underlying host galaxies. UPDATE THIS. All spectra have been made publicly available in the reduced form used in this paper.

Our sample serves the purpose to further characterize the environments of GRBs that was also much advanced by the previous surveys based primarily on lower-resolution spectrographs. The most striking result found is that GRBs typically are located behind very large column densities of neutral hydrogen. Only after observing more than 12000 damped Lyman- α absorbers (DLAs) towards about 10^5 quasars have a handful such systems with $\log(N_{\text{HI}}/\text{cm}^{-2}) > 22$ been identified (e.g., five in Noterdaeme et al. 2012). Long GRB afterglow spectra, by contrast, reveal such systems in the majority of cases (Jakobsson et al. 2006; Fynbo et al. 2009, and this work). With afterglow spectroscopy (throughout the electromagnetic spectrum from X-rays to the sub-mm) we hence characterize the properties of star-forming galaxies over cosmic history in terms of redshifts, metallicities, molecular contents, ISM temperatures, UV-flux densities, extinction curves, etc. A number of independent papers have been published or submitted for publication focusing on many of these specific issues of our sample such as extinction curves [see also Fynbo et al. (2014); ?](??), emission lines from the underlying host galaxies (Krühler et al. 2015), the frequency of intervening Mg II absorbers (?), and escape of ionizing radiation (?).

It seems important to end this paper by stressing that the potential of using GRB sightlines as probes is far from fully harvested. The sample of sightlines probed by our spectra is not representative for all GRB sightlines as we have shown and consis-

Table 2: Hydrogen column densities for all bursts exhibiting Ly α absorption in the spectral coverage of X-shooter. Corresponding fits are shown in Fig. 3.

GRB	Hydrogen Column
GRB 090809A	21.7 ± 0.2
GRB 090926A	21.55 ± 0.10
GRB 100219A	21.20 ± 0.20
GRB 100425A	21.10 ± 0.20
GRB 110128A	22.00 ± 0.15
GRB 110818A	21.9 ± 0.4
GRB 111008A	22.40 ± 0.10
GRB 111107A	21.0 ± 0.2
GRB 120119A	22.7 ± 0.2
GRB 120327A	22.0 ± 0.15
GRB 120404A	20.7 ± 0.3
GRB 120712A	19.95 ± 0.15
GRB 120716A	22.00 ± 0.15
GRB 120815A	22.05 ± 0.10
GRB 120909A	21.70 ± 0.10
GRB 121024A	21.85 ± 0.10
GRB 121027A	22.8 ± 0.3
GRB 121201A ^a	22.0 ± 0.3
GRB 121229A	21.7 ± 0.2
GRB 130408A	21.8 ± 0.1
GRB 130427B	21.9 ± 0.3
GRB 130606A	19.91 ± 0.02
GRB 130612A	22.1 ± 0.2
GRB 131011A	22.0 ± 0.3
GRB 131117A	20.0 ± 0.3
GRB 140311A	22.40 ± 0.15
GRB 140430A	21.8 ± 0.3
GRB 140515A	19.0 ± 0.5
GRB 140614A	21.6 ± 0.3
GRB 141028A	20.6 ± 0.15
GRB 141109A	22.1 ± 0.1
GRB 150206A	21.7 ± 0.4
GRB 150403A	21.8 ± 0.2
GRB 150915A ^a	21.2 ± 0.3
GRB 151021A	22.2 ± 0.2
GRB 151027B	20.5 ± 0.2
GRB 160203A	21.75 ± 0.10
GRB 160410A ^b	21.2 ± 0.2
GRB 161014A	21.4 ± 0.3
GRB 161023A	20.96 ± 0.05

Notes. ^(a) Has Ly α emission in the trough. ^(b) Short burst.

tent with earlier findings from samples based on low-resolution spectroscopy (e.g., Fynbo et al. 2009) and from studies of complete samples of GRB host galaxies (Perley et al. 2016). Krühler et al. (2013) convincingly argue, that very rich sightlines like that probed by the remarkable GRB 080607 (?) are probably significantly more frequent than in the sightlines sampled by our spectra. However, with current instrumentation these sightlines are out of reach except under very fortunate circumstances as in the case of GRB 080607 when the afterglow could be observed only a few minutes after the burst with a 10-m class telescope. Observations of such sightlines with X-shooter-like spectrographs on the next generation of 20–40-m telescopes is likely to be very rewarding.

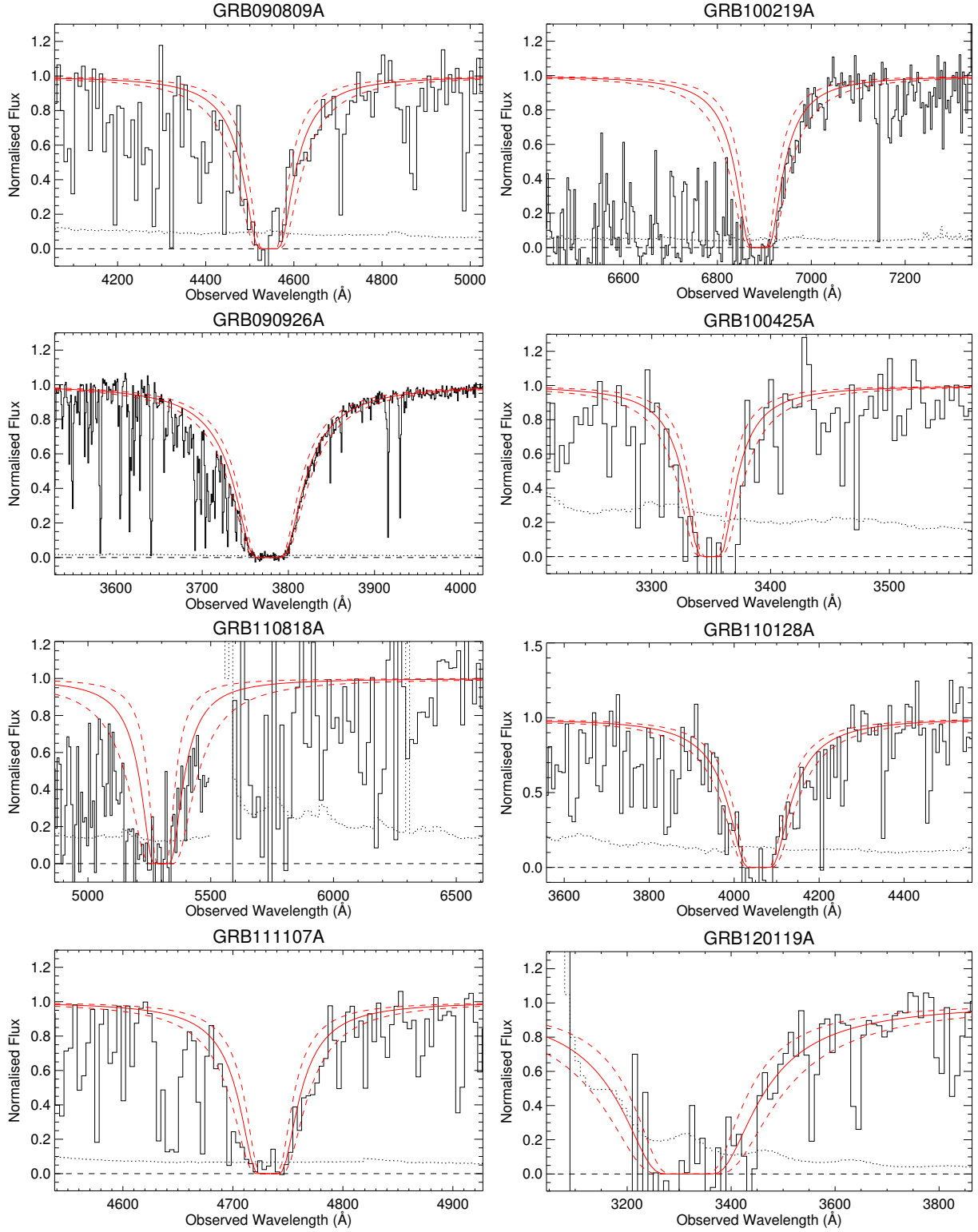


Fig. 3: Measurements of the hydrogen column-densities for all bursts with a clear Lyman alpha absorption system. In solid black is shown the spectrum with black dotted giving the corresponding 1- σ error. Black dashed shows zero flux density. The solid red line is the absorption of column density equal to the value presented in Tab. ?? with the 1- σ interval shown with dashed lines.

Acknowledgements. *** We should add an ode to Neil Gehrels here ***. JPUF, BMJ and DX acknowledge support from the ERC-StG grant EGG-278202. The Dark Cosmology Centre is funded by the Danish National Research Foundation. TK acknowledges support by the European Commission under the Marie Curie Intra-European Fellowship Programme in FP7. AdUP acknowledges support by the European Commission under the Marie Curie Career Integration Grant programme (FP7-PEOPLE-2012-CIG 322307). This work made use of data supplied by the UK *Swift* Science Data Centre at the University of Leicester. Finally, we acknowledge expert support from the ESO staff at the Paranal and La Silla observatories in obtaining these target of opportunity data.

References

- Abrarov S. M., Quine B. M., 2015a, *J. Math. Res.*, 7, 44
 Abrarov S. M., Quine B. M., 2015b, *J. Math. Res.*, 7, 163
 Benner D. C., Rinsland C. P., Devi V. M., Smith M. A. H., Atkins D., 1995, *JQSRT*, 53, 705
 Bloom J. S., Kulkarni S. R., Djorgovski S. G., 2002, *AJ*, 123, 1111
 Bufano F., et al., 2012, *ApJ*, 753, 67
 Cardelli J. a., Clayton G. C., Mathis J. S., 1989, *ApJ*, 345, 245
 Cobb B. E., Bloom J. S., Perley D. A., Morgan A. N., Cenko S. B., Filippenko A. V., 2010, *ApJ*, 718, L150
 D’Elia V., Stratta G., 2011, *A&A*, 532, A48
 D’Elia V., et al., 2010, *A&A*, 523, A36
 D’Elia V., et al., 2014, *A&A*, 564, A38
 De Ugarte Postigo A., Thöne C. C., Goldoni P., Fynbo J. P. U., 2011, *AN*, 332, 297
 Filippenko A. V., 1982, *PASP*, 94, 715
 Fong W., et al., 2013, *ApJ*, 769, 56
 Freudling W., Romaniello M., Bramich D. M., Ballester P., Forchi V., García-Dabó C. E., Mochler S., Neeser M. J., 2013, *A&A*, 559, A96
 Friis M., et al., 2015, *MNRAS*, 451, 167
 Fruchter A. S., et al., 2006, *Natur*, 441, 463
 Fynbo J. P. U., et al., 2009, *ApJS*, 185, 175
 Fynbo J. P. U., et al., 2014, *A&A*, 12, 1
 Ginsburg A., et al., 2016, *astroquery* v0.3.1, doi:10.5281/ZENODO.44961, <https://github.com/astroquery/astroquery>
 Goldoni P., Royer F., François P., Horrobin M., Blanc G., Vernet J., Modigliani A., Larsen J., 2006, *Ground-based Airborne Instrum. Astron. Ed. by McLean*, 6269, 80
 Hamuy M., Suntzeff N. B., Heathcote S. R., Walker A. R., Gigoux P., Phillips M. M., 1994, *PASP*, 106, 566
 Hartoog O. E., et al., 2013, *MNRAS*, 430, 2739
 Hartoog O. E., et al., 2015, *A&A*, 580, A139
 Hogg D. W., Fruchter A. S., 1999, *ApJ*, 520, 54
 Horne K., 1986, *PASP*, 98, 609
 Jakobsson P., et al., 2006, *A&A*, 460, L13
 Jakobsson P., et al., 2012, *ApJ*, 752, 62
 Jones E., Oliphant T., Peterson P., 2001, *SciPy: Open source scientific tools for Python*, <http://www.scipy.org/>
 Jones A., Noll S., Kausch W., Szyszka C., Kimeswenger S., 2013, *A&A*, 560, A91
 Kausch W., et al., 2015, *A&A*, 576, A78
 Krühler T., et al., 2013, *A&A*, 557, A18
 Krühler T., et al., 2015, *A&A*, 581, A125
 Letchworth K. L., Benner D. C., 2007, *JQSRT*, 107, 173
 Levan A. J., et al., 2014, *ApJ*, 781, 13
 McGuire J. T. W., et al., 2016, *ApJ*, 825, 135
 Modigliani A., et al., 2010, *SPIE Astron. Telesc. + Instrum.*, 7737, 773728
 Moffat A. F. J., 1969, *A&A*, 3, 455
 Noll S., Kausch W., Barden M., Jones A. M., Szyszka C., Kimeswenger S., Vinther J., 2012, *A&A*, 543, A92
 Noterdaeme P., et al., 2012, *A&A*, 547, L1
 Pagnini G., Mainardi F., 2010, *JCoAM*, 233, 1590
 Perley D. A., et al., 2016, *ApJ*, 817, 7
 Rafelski M., Neeleman M., Fumagalli M., Wolfe A. M., Prochaska J. X., 2014, *ApJ*, 782, L29
 Robertson B. E., Ellis R. S., 2012, *ApJ*, 744, 95
 Salvaterra R., Campana S., Chincarini G., Tagliaferri G., Covino S., 2007, *Mon. Not. R. Astron. Soc. Lett.*, 380, L45
 Salvaterra R., et al., 2009, *Natur*, 461, 1258
 Salvaterra R., et al., 2012, *ApJ*, 749, 68
 Schlafly E. F., Finkbeiner D. P., 2011, *ApJ*, 737, 103
 Schlegel D. J., Finkbeiner D. P., Davis M., 1998, *ApJ*, 500, 525
 Schulze S., Malesani D., Cucchiara A., Tanvir N. R., Krühler T., Postigo A. D. U., Leloudas G., 2014, *A&A*, 102, 1
 Selsing J., Fynbo J. P. U., Christensen L., Krogager J.-K., 2015, *A&A*, 87, 14
 Smette A., et al., 2015, *A&A*, 576, A77
 Sparre M., et al., 2011, *ApJ*, 735, L24
 Sparre M., et al., 2014, *ApJ*, 785, 150
 Starling R. L. C., et al., 2011, *MNRAS*, 411, 2792
 Tanvir N. R., et al., 2009, *Natur*, 461, 1254
 Tanvir N. R., et al., 2012, *ApJ*, 754, 46
 Tepper García T., 2006, *MNRAS*, 369, 2025
 Thöne C. C., et al., 2013, *MNRAS*, 428, 3590
 Trujillo I., Aguerri J. A. L., Cepa J., Gutiérrez C. M., 2001, *MNRAS*, 328, 977
 Vergani S. D., et al., 2011, *A&A*, 535, A127
 Vernet J., et al., 2009, *Proc. Int. Astron. Union*, 5, 535
 Vernet J., et al., 2011, *A&A*, 536, A105
 Wiersema K., et al., 2012, *MNRAS*, 426, 2
 de Ugarte Postigo A., et al., 2010, *A&A*, 513, A42
 van Dokkum P. G., 2001, *PASP*, 113, 1420

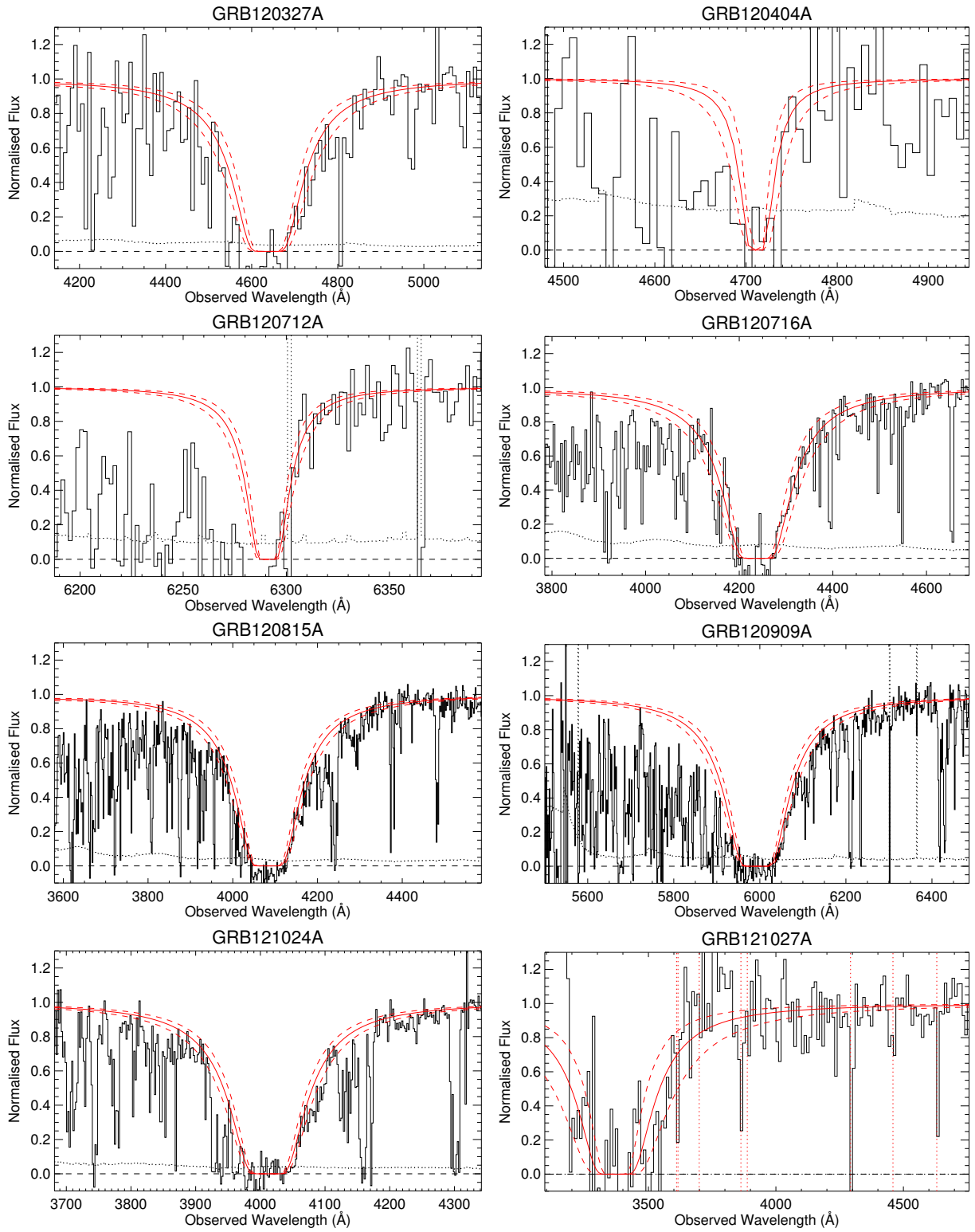


Fig. 3. continued.

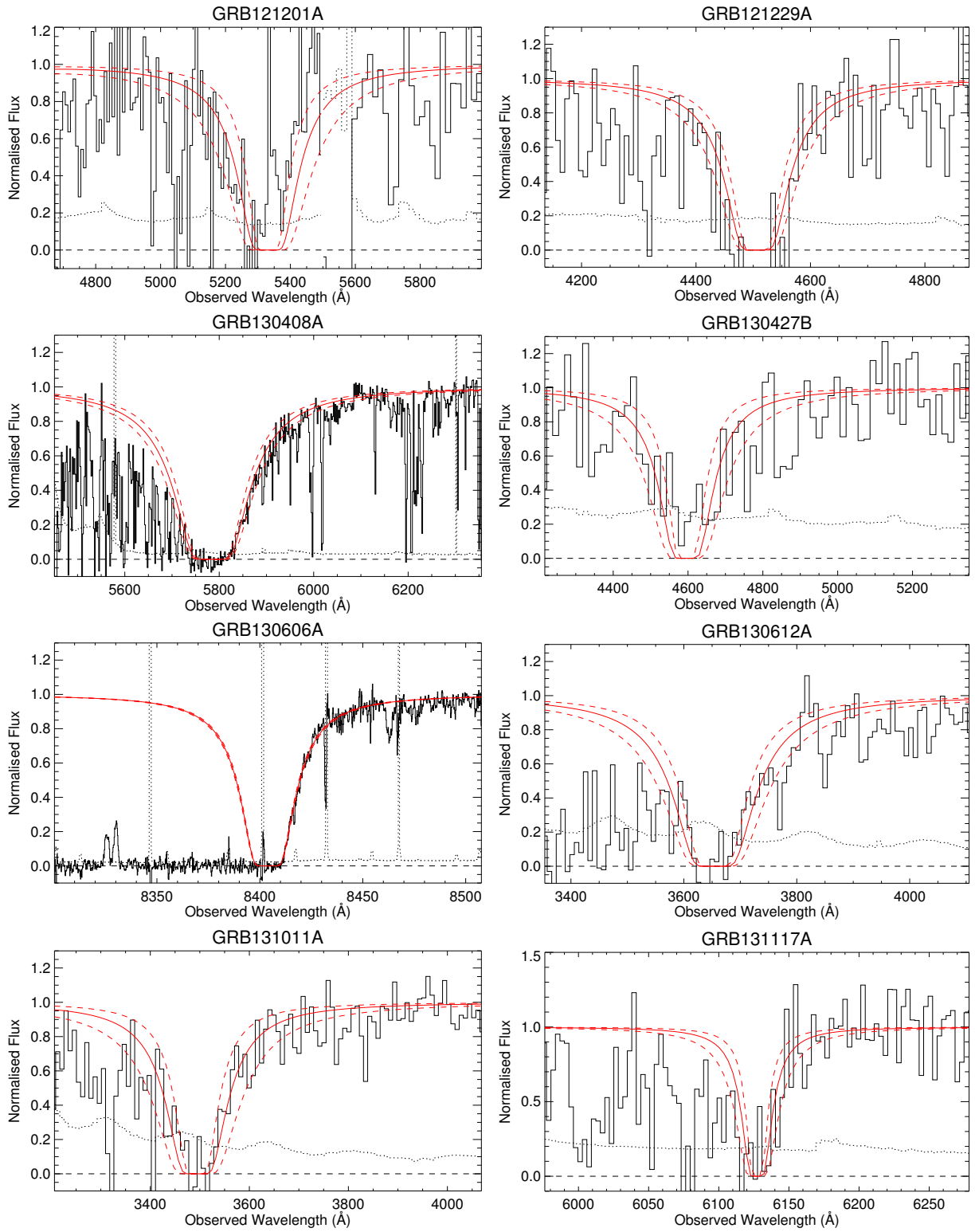


Fig. 3. continued.

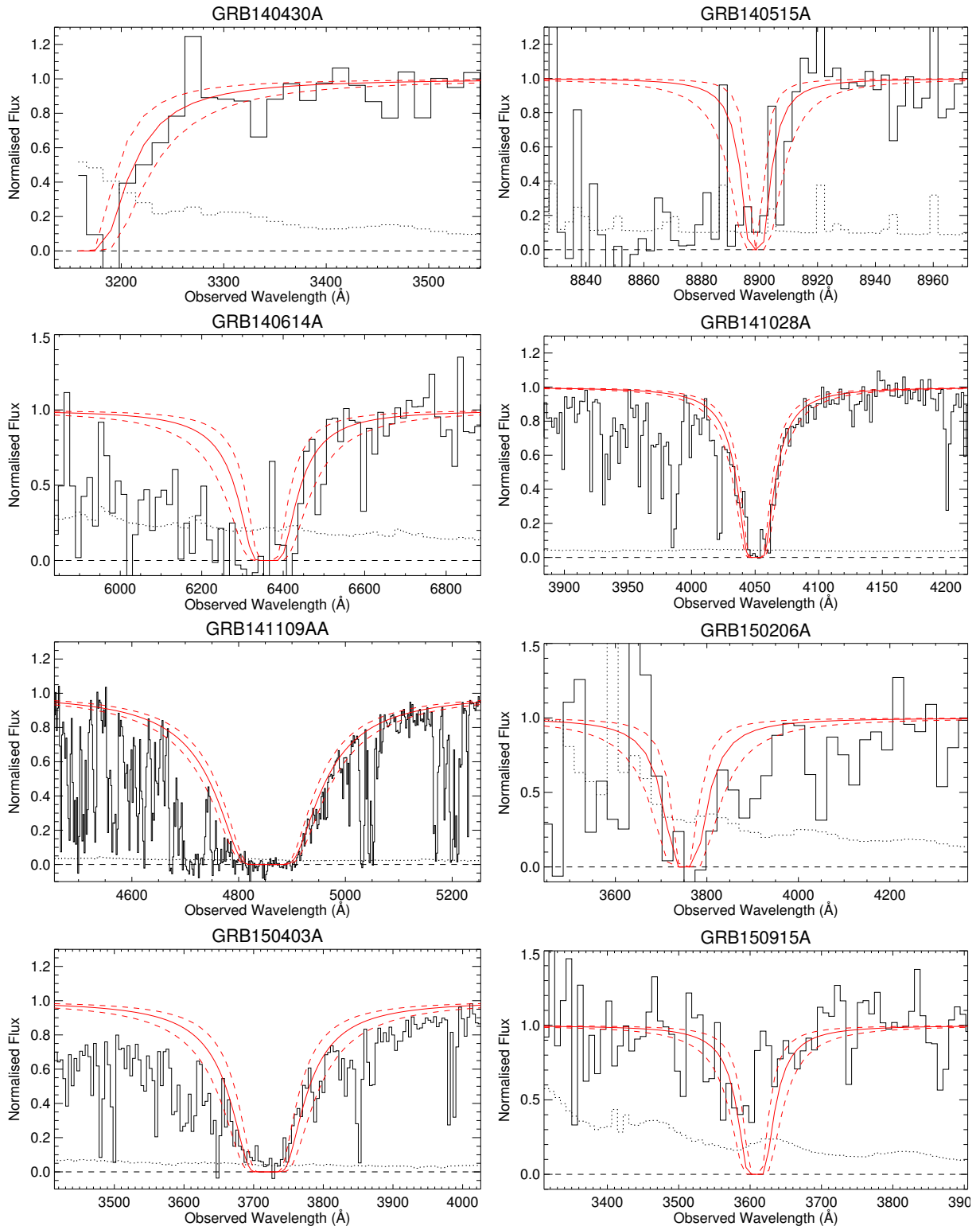


Fig. 3. continued.

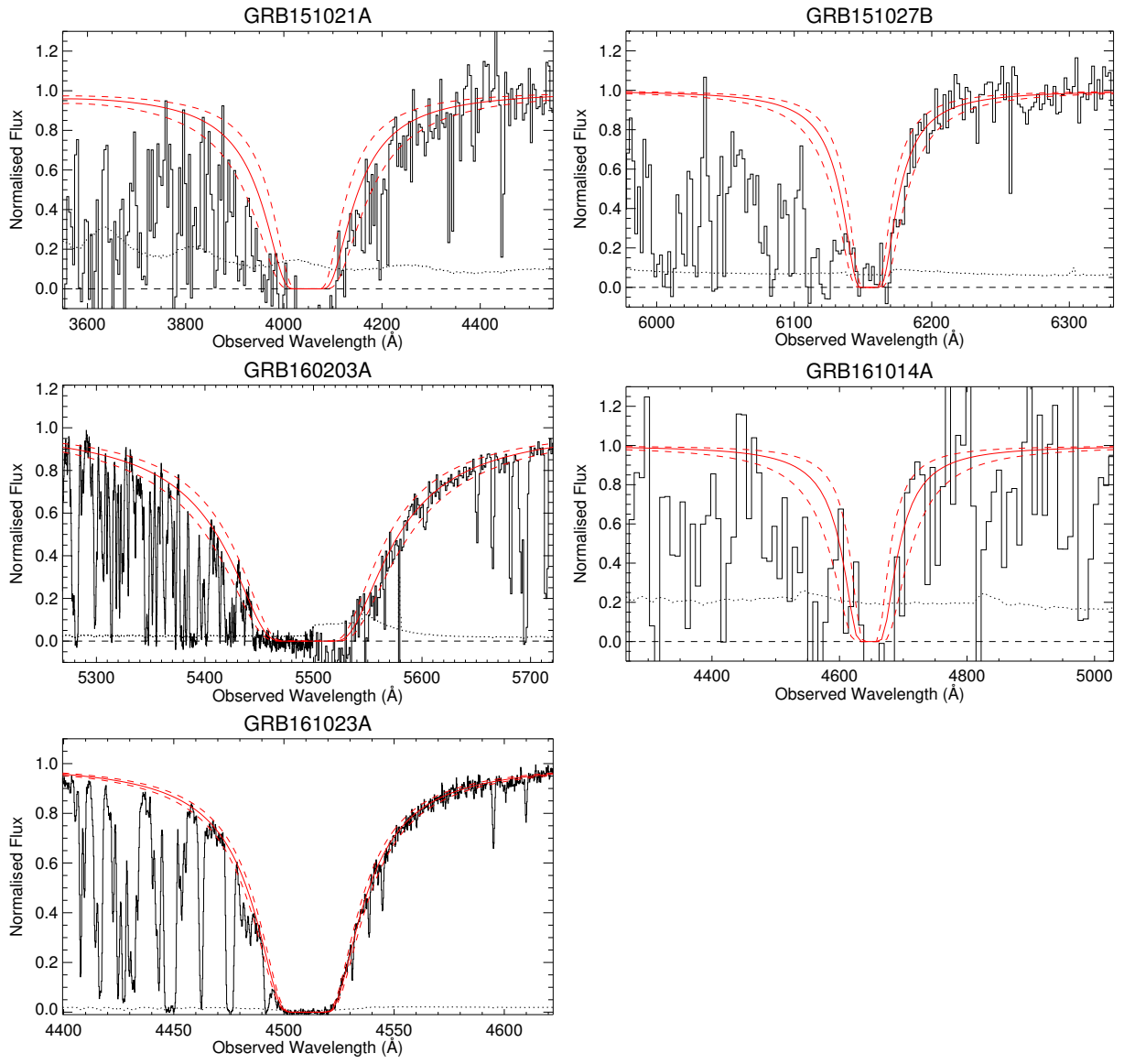


Fig. 3. continued.

Table 1: The full sample of afterglows or hosts observed in the program. We here list the burst names and details of the spectroscopic observations. The exposure times and slit widths are given in the order UVB/VIS/NIR. The column Δt shows the time after trigger when the spectroscopic observation was started. Mag_{acq} gives the approximate magnitude (typically in the R -band) of the afterglow in the acquisition image.

GRB	Exptime	Slit width	Airmass	Seeing	Δt	Mag_{acq}	Redshift	Ref
	(ks)	(arcsec)		(arcsec)	(hr)			
GRB090313 ^a	6.9/6.9/6.9	1.0/0.9/0.9	1.2–1.4	1.0	45	21.6	3.3736	(1)
GRB090530 ^a	4.8/4.8/4.8	1.0/1.2/1.2	1.6–2.2	1.5	20	22	1.266	(2)
GRB090809 ^a	7.2/7.2/7.2	1.0/0.9/0.9	1.2–1.1	0.9	10.2	21	2.737	(2,3)
GRB090926 ^a	7.2/7.2/7.2	1.0/0.9/0.9	1.4–1.5	0.9	22	17.9	2.1062	(4)
GRB091018	2.4/2.4/2.4	1.0/0.9/0.9	2.1–1.8	0.8	3.5	19.1	0.9710	(5)
GRB091127	6.0/6.0/6.0	1.0/0.9/0.9	1.1–1.2	1.0	101	21.2	0.490	(6)
GRB100205A	10.8/10.8/10.8	1.0/0.9/0.9	1.9–1.8	1.0	71	–	–	(2)
GRB100219A	4.8/4.8/4.8	1.0/0.9/0.9	1.3–1.1	0.7	12.5	23	4.667	(7)
GRB100316B	2.4/2.4/2.4	1.0/0.9/0.9	2.0–2.4	0.7	0.7	18.2	1.18	(2)
GRB100316D-1 ^(b)	3.6/3.6/1.8	1.0/0.9/0.9	1.2–1.3	1.0	10	21.5	0.059	(8)
GRB100316D-2	2.4/2.4/2.4	1.0/0.9/0.9	1.1–1.2	1.0	58	20.2	0.059	(8)
GRB100316D-3	2.6/2.6/3.2	1.0/0.9/0.9	1.1–1.2	1.1	79	19.9	0.059	(8)
GRB100316D-4	2.6/2.6/3.2	1.0/0.9/0.9	1.1–1.2	1.2	101	19.9	0.059	(8)
GRB100418A-1	4.8/4.8/4.8	1.0/0.9/0.9	1.6–1.3	0.7	8.4	18.1	0.624	(9)
GRB100418A-2	4.8/4.8/4.8	1.0/0.9/0.9	1.2–1.3	0.6	34	19.2	0.624	(9)
GRB100418A-3	4.8/4.8/4.8	1.0/0.9/0.9	1.2–1.4	0.7	58	–	0.624	(9)
GRB100424A ^c	4.8/4.8/4.8	1.0/0.9/0.9	1.1–1.2	0.8	–	–	2.465	(2)
GRB100425A	2.4/2.4/2.4	1.0/0.9/0.9	1.5–1.3	0.7	4.0	20.6	1.755	(2,3)
GRB100615A ^c	4.8/4.8/4.8	1.0/0.9/0.9	1.0–1.1	0.8	–	–	1.398	(2)
GRB100621A	2.4/2.4/2.4	1.0/0.9/0.9	1.3–1.4	1.0	7.1	–	0.542	(2)
GRB100625A ^c	4.8/4.8/4.8	1.0/0.9/0.9	1.1–1.0	0.8	13	–	0.452	(2)
GRB100724A ^(d)	4.2/4.2/4.2	1.0/0.9/0.9	1.5–2.3	0.7	0.2	–	1.288	(2)
GRB100728B ^(e)	7.2/7.2/7.2	1.0/0.9/0.9	1.5–1.1	0.5	22	23	2.106	(2)
GRB100814A-1 ^(d)	0.9/0.9/0.9	1.0/0.9/0.9	1.9–1.7	0.5	0.9	19	1.439	(2)
GRB100814A-2	4.8/4.8/2.4	1.0/0.9/0.9	1.5–1.2	0.6	2.1	19	1.439	(2)
GRB100814A-3	4.8/4.8/2.4	1.0/0.9/0.9	1.2–1.0	0.6	98	20	1.439	(2)
GRB100816A ^(f)	4.8/4.8/2.4	1.0/0.9/0.9	1.8–1.6	0.8	28.4	–	0.805	(2)
GRB100901A	2.4/2.4/2.4	1.0/0.9/0.9	1.5–1.5	1.5	66	–	1.408	(10)
GRB101219A	7.2/7.2/7.2	1.0/0.9/0.9	1.1–1.7	2.0	3.7	–	0.718	(2)
GRB101219B-1	4.8/4.8/4.8	1.0/0.9/0.9	1.6–2.6	1.3	11.6	20	0.552	(11)
GRB101219B-2	7.2/7.2/7.2	1.0/0.9/0.9	1.2–2.0	0.8	394	22.7	0.552	(11)
GRB101219B-3	7.2/7.2/7.2	1.0/0.9/0.9	1.4–2.1	0.9	886	–	0.552	(11)
GRB110128A	7.2/7.2/7.2	1.0/0.9/0.9	2.0–1.6	0.9	5.5	22.5	2.339	(2)
GRB110407A	9.6/9.6/9.6	1.0/0.9/0.9	1.4–1.3	2.0	12.4	23	–	(2)
GRB110709B ^{a c}	7.2/7.2/7.2	1.0/0.9/0.9	1.6–1.1	1.0	–	–	–	(2)
GRB110715A	0.6/0.6/0.6	1.0/0.9/0.9	1.1–1.1	1.7	12.3	18.5	0.82	(2)
GRB110721A	2.4/2.4/2.4	1.0/0.9/0.9	1.2–1.4	2.4	–	–	0.382	(2)
GRB110808A	2.4/2.4/2.4	1.0/0.9/0.9	1.2–1.1	1.1	3.0	21.2	1.3488	(2)
GRB110818A	4.8/4.8/4.8	1.0/0.9/0.9	1.3–1.3	1.0	6.2	22.3	3.36	(2)
GRB111005A ^c	1.2/1.2/1.2	1.0/0.9/0.9	1.3–1.3	0.7	–	–	0.013?	(2)
GRB111008A-1	8.8/8.8/8.4	1.0/0.9/0.9	1.1–1.0	1.2	8.5	21?	4.9898	(12)
GRB111008A-2	8.0/8.0/7.2	1.0/0.9/0.9	1.3–1.0	1.0	20.1	22?	4.9898	(12)
GRB111107A	4.8/4.8/4.8	1.0/0.9/0.9	1.8–1.5	0.7	5.3	21.5	2.893	(2)
GRB111117A ^(f)	4.8/4.8/4.8	1.0/0.9/0.9	1.5–1.4	0.6	38	–	1.3?	(2)
GRB111123A-1	6.2/6.6/6.6	1.0/0.9/0.9	1.6–1.1	1.0	12.2	>24	3.1516	(2)
GRB111123A-2 ^c	2.4/2.4/2.4	1.0/0.9/0.9	1.0–1.0	0.5	–	–	3.1516	(2)
GRB111129A	3.6/3.6/3.6	1.0/0.9/0.9	1.6–2.1	1.7	–	–	–	(2)
GRB111209A-1	4.8/4.8/4.8	1.0/0.9/0.9	1.1–1.2	0.8	17.7	20.1	0.677	(13)
GRB111209A-2	9.6/9.6/9.6	1.0/0.9/0.9	1.2–2.0	0.8	497	23	0.677	(13)
GRB111211A ^a	2.4/2.4/2.4	1.0/0.9/0.9	1.4–1.6	0.6	31	19.5	0.478	(2)
GRB111228A	2.4/2.4/2.4	1.0/0.9/0.9	1.4–1.4	0.9	15.9	20.1	0.716	(2)
GRB120118B ^c	3.6/3.6/3.6	1.0/0.9/0.9	1.1–1.0	1.0	–	–	2.943	(2)
GRB120119A-1	2.4/2.4/2.4	1.0/0.9/0.9	1.1–1.1	0.6	1.4	17	1.728	(2)
GRB120119A-2	1.2/1.2/1.2	1.0/0.9/0.9	1.8–1.9	0.6	4.5	20	1.728	(2)
GRB120119A-3 ^c	4.8/4.8/4.8	1.0/0.9/0.6JH	1.0–1.1	1.1	–	–	1.728	(2)
GRB120211A-1	4.8/4.8/4.8	1.0/0.9/0.9	1.1–1.4	1.0	–	–	2.346	(2)

Table 1: The full sample of afterglows or hosts observed in the program (continued).

GRB	Exptime	Slit width	Airmass	Seeing	Δt	Mag _{acq}	Redshift	Ref
	(ks)	(arcsec)		(arcsec)	(hr)			
GRB120211A-2	3.6/3.6/3.6	1.0/0.9/0.9	1.1–1.2	1.3	–	–	2.346	(2)
GRB120224A	2.4/2.4/2.4	1.0/0.9/0.9	1.7–2.1	1.4	19.8	22.3	1.10	(2)
GRB120311A ^a	2.4/2.4/2.4	1.0/0.9/0.9	1.6–1.4	0.6	3.7	21.6	0.350	(2)
GRB120327A-1	2.4/2.4/2.4	1.0/0.9/0.9	1.6–1.4	0.5	2.1	18.8	2.815	(14)
GRB120327A-2	4.2/4.2/4.2	1.0/0.9/0.9	1.0–1.1	1.0	29	22.5	2.815	(14)
GRB120404A	9.6/9.6/9.6	1.0/0.9/0.9JH	1.7–1.3	1.3	15.7	21.3	2.876	(2)
GRB120422A	4.8/4.8/4.8	1.0/0.9/0.9	1.3–1.3	0.6	16.5	22.0	0.283	(15)
GRB120712A	4.8/4.8/4.8	1.0/0.9/0.9	1.5–2.5	1.3	10.4	21.5	4.175	(2)
GRB120714B	4.8/4.8/4.8	1.0/0.9/0.9JH	1.5–1.2	1.2	7.8	22.1	0.398	(2)
GRB120716A ^a	3.6/3.6/3.6	1.0/0.9/0.9JH	1.8–2.6	1.0	62	20.9	2.486	(2)
GRB120722A ^(b)	4.8/4.8/4.8	1.0/0.9/0.9	1.3–1.3	1.1	10.3	23.6	0.959	(2)
GRB120805A ^(b)	3.6/3.6/3.6	1.0/0.9/0.9JH	1.3–1.7	0.9	218	–	2.8?	(2)
GRB120815A	2.4/2.4/2.4	1.0/0.9/0.9	1.3–1.4	0.6	1.69	18.9	2.358	(16)
GRB120909A	1.2/1.2/1.2	1.0/0.9/0.9	1.6–1.6	1.4	1.7	21	3.929	(2)
GRB120923A	9.6/9.6/9.6	1.0/0.9/0.9JH	1.2–1.4	1.0	18.5	–	≥ 8	(2)
GRB121024A	2.4/2.4/2.4	1.0/0.9/0.9	1.2–1.1	0.6	1.8	20	2.300	(17)
GRB121027A	8.4/8.4/8.4	1.0/0.9/0.9	1.3–1.3	0.9	69.4	21.15	1.773	(2)
GRB121201A	4.8/4.8/4.8	1.0/0.9/0.9JH	1.1–1.1	0.9	12.9	23	3.385	(2)
GRB121229A	4.8/4.8/4.8	1.0/0.9/0.9JH	1.4–1.2	1.4	2.0	21.5	2.707	(2)
GRB130131B ^c	7.2/7.2/7.2	1.0/0.9/0.9JH	1.3–1.6	0.8	–	–	2.539	(2)
GRB130408A	1.2/1.2/1.2	1.0/0.9/0.9	1.0–1.0	1.0	1.9	20	3.758	(2)
GRB130418A	1.2/1.2/1.2	1.0/0.9/0.9	1.4–1.3	1.3	4.6	18.5	1.218	(2)
GRB130427A	1.2/1.2/1.2	1.0/0.9/0.9JH	1.8–1.8	0.8	16.5	19	0.340	(18)
GRB130427B	1.2/1.2/1.2	1.0/0.9/0.9JH	1.2–1.0	0.8	20.3	22.7	2.78	(2)
GRB130603B ^(f)	2.4/2.4/2.4	1.0/0.9/0.9	1.4–1.4	1.1	8.2	21.5	0.356	(19)
GRB130606A	4.2/4.2/4.2	1.0/0.9/0.9JH	1.7–1.9	1.1	7.1	19	5.91	(20)
GRB130612A	1.2/1.2/1.2	1.0/0.9/0.9	1.3–1.3	1.4	1.1	21.5	2.006	(2)
GRB130615A	1.2/1.2/1.2	1.0/0.9/0.9	2.1–2.2	1.0	0.8	21	3?	(2)
GRB130701A	1.2/1.2/1.2	1.0/0.9/0.9JH	2.0–2.0	1.6	5.5	19.9	1.155	(2)
GRB131011A	9.9/9.9/9.9	9.9/9.9/9.9QQ	9.9–9.9				1.874	(2)
GRB131030A	9.9/9.9/9.9	9.9/9.9/9.9QQ	9.9–9.9				1.296	(2)
GRB131103A	9.9/9.9/9.9	9.9/9.9/9.9QQ	9.9–9.9		5.8	20.48	0.599	(2)
GRB131105A	9.9/9.9/9.9	9.9/9.9/9.9QQ	9.9–9.9		1.3	22.4	1.686	(2)
GRB131117A	9.9/9.9/9.9	9.9/9.9/9.9QQ	9.9–9.9		1	20	4.042	(2)
GRB131231A	9.9/9.9/9.9	9.9/9.9/9.9QQ	9.9–9.9		20.2	18.5	0.642	(2)
GRB140114A	9.9/9.9/9.9	9.9/9.9/9.9QQ	9.9–9.9				2.8	(2)
GRB140213A	9.9/9.9/9.9	9.9/9.9/9.9QQ	9.9–9.9		5.8	19.5	1.208	(2)
GRB140301A	9.9/9.9/9.9	9.9/9.9/9.9QQ	9.9–9.9		9	23.1	1.416	(2)
GRB140311A	9.9/9.9/9.9	9.9/9.9/9.9QQ	9.9–9.9				4.95	(2)
GRB140430A	9.9/9.9/9.9	9.9/9.9/9.9QQ	9.9–9.9		2.5	19	1.601	(2)
GRB140506A-1	9.9/9.9/9.9	9.9/9.9/9.9QQ	9.9–9.9		8.8	20.9	0.889	(2)
GRB140506A-2	9.9/9.9/9.9	9.9/9.9/9.9QQ	9.9–9.9		–	–	0.889	(2)
GRB140515A	9.9/9.9/9.9	9.9/9.9/9.9QQ	9.9–9.9				6.32	(2)
GRB140614A	9.9/9.9/9.9	9.9/9.9/9.9QQ	9.9–9.9		3.8	21.5	4.233	(2)
GRB140622A	9.9/9.9/9.9	9.9/9.9/9.9QQ	9.9–9.9				0.959	(2)
GRB141028A	9.9/9.9/9.9	9.9/9.9/9.9QQ	9.9–9.9		15.4	20	2.332	(2)
GRB141031A-1	9.9/9.9/9.9	9.9/9.9/9.9QQ	9.9–9.9					(2)
GRB141031A-2	9.9/9.9/9.9	9.9/9.9/9.9QQ	9.9–9.9					(2)
GRB141109A-1	9.9/9.9/9.9	9.9/9.9/9.9QQ	9.9–9.9		1.9	19.2	2.993	(2)
GRB141109A-2	9.9/9.9/9.9	9.9/9.9/9.9QQ	9.9–9.9				2.993	(2)
GRB150206A	9.9/9.9/9.9	9.9/9.9/9.9QQ	9.9–9.9		10	21.9	2.087	(2)
GRB150301B	9.9/9.9/9.9	9.9/9.9/9.9QQ	9.9–9.9				1.5169	(2)
GRB150403A	9.9/9.9/9.9	9.9/9.9/9.9QQ	9.9–9.9		10.8	19.1	2.06	(2)
GRB150423A	9.9/9.9/9.9	9.9/9.9/9.9QQ	9.9–9.9				1.394	(2)
GRB150428A	9.9/9.9/9.9	9.9/9.9/9.9QQ	9.9–9.9					(2)
GRB150514A	9.9/9.9/9.9	9.9/9.9/9.9QQ	9.9–9.9		28.4	19.5	0.807	(2)
GRB150518A	9.9/9.9/9.9	9.9/9.9/9.9QQ	9.9–9.9				0.256	(2)
GRB150616A	9.9/9.9/9.9	9.9/9.9/9.9QQ	9.9–9.9					(2)
GRB150727A	9.9/9.9/9.9	9.9/9.9/9.9QQ	9.9–9.9				0.313	(2)

Table 1: The full sample of afterglows or hosts observed in the program (continued).

GRB	Exptime	Slit width	Airmass	Seeing	Δt	Mag _{acq}	Redshift	Ref
	(ks)	(arcsec)		(arcsec)	(hr)			
GRB150821A	9.9/9.9/9.9	9.9/9.9/9.9QQ	9.9–9.9		0.2	16	0.755	(2)
GRB150910A	9.9/9.9/9.9	9.9/9.9/9.9QQ	9.9–9.9				1.359	(2)
GRB150915A	9.9/9.9/9.9	9.9/9.9/9.9QQ	9.9–9.9		3.3	23	1.968	(2)
GRB151021A	9.9/9.9/9.9	9.9/9.9/9.9QQ	9.9–9.9		0.75	18.2	2.33	(2)
GRB151027B	9.9/9.9/9.9	9.9/9.9/9.9QQ	9.9–9.9		5	20.5	4.063	(2)
GRB151029A	9.9/9.9/9.9	9.9/9.9/9.9QQ	9.9–9.9		1	20	1.423	(2)
GRB151031A	9.9/9.9/9.9	9.9/9.9/9.9QQ	9.9–9.9		0.3	20.4	1.167	(2)
GRB160117B	9.9/9.9/9.9	9.9/9.9/9.9QQ	9.9–9.9		13.5	21	0.87	(2)
GRB160203A	9.9/9.9/9.9	9.9/9.9/9.9QQ	9.9–9.9		0.3	18	3.52	(2)
GRB160228A	9.9/9.9/9.9	9.9/9.9/9.9QQ	9.9–9.9				1.64	(2)
GRB160303A	9.9/9.9/9.9	9.9/9.9/9.9QQ	9.9–9.9				-	(2)
GRB160314A	9.9/9.9/9.9	9.9/9.9/9.9QQ	9.9–9.9				0.726	(2)
GRB160410A	9.9/9.9/9.9	9.9/9.9/9.9QQ	9.9–9.9		0.15	20.3	1.717	(2)
GRB160425A	9.9/9.9/9.9	9.9/9.9/9.9QQ	9.9–9.9				0.555	(2)
GRB160625B	9.9/9.9/9.9	9.9/9.9/9.9QQ	9.9–9.9		30	19.1	1.406	(2)
GRB160804A-1	2.4/2.4/2.4	1.0/0.9/0.9JH	1.3–1.4	–	22.4	21.2	0.736	(2)
GRB160804A-2 ^c	3.6/3.6/3.6	1.0/0.9/0.9JH	1.8–1.9	–	–	–	0.736	(2)
GRB161001A	9.9/9.9/9.9	9.9/9.9/9.9QQ	9.9–9.9					(2)
GRB161007A ^c	2.4/2.4/2.4	1.0/0.9/0.9JH	1.5–1.7	0.8	323	–	???	(2)
GRB161014A	4.8/4.8/4.8	1.0/0.9/0.9JH	1.1–1.2	0.6	11.6	21.4	2.823	(2)
GRB161023A	9.9/9.9/9.9	9.9/9.9/9.9QQ	9.9–9.9		3	17.5	2.710	(2)

Notes. ^(a) Not part of the statistical sample ^(b) Spectrum dominated by light from the host galaxy ^(c) Spectrum of the host galaxy taken long after the burst ^(d) RRM observation ^(e) ADC malfunction during observation ^(f) Short burst

References. (1) de Ugarte Postigo et al. (2010); (2) This work ; (3) Skuladottir (2010); (4) D’Elia et al. (2010); (5) Wiersema et al. (2012); (6) Vergani et al. (2011); Cobb et al. (2010); (7) Thöne et al. (2013); (8) Bufano et al. (2012) ; (9) De Ugarte Postigo et al. (2011) ; (10) Hartoog et al. (2013); (11) Sparre et al. (2011); (12) Sparre et al. (2014); (13) Levan et al. (2014); (14) D’Elia et al. (2014); (15) Schulze et al. (2014); (16) Krühler et al. (2013); (17) Friis et al. (2015)

Appendix A: The complex error function and the Voigt profile

When modeling the spectral PSF, we need to evaluate the Voigt-profile. The Voigt profile, which is the convolution of the Gaussian and Lorentzian profiles, can, centered at zero, be written as (Pagnini & Mainardi 2010)

$$\begin{aligned} V(\lambda, \sigma, \gamma) &= G(\lambda, \sigma) \otimes L(\lambda, \gamma) \\ &= \int_{-\infty}^{\infty} G(\xi, \sigma) L(\lambda - \xi, \gamma) d\xi \\ &= \int_{-\infty}^{\infty} \frac{1}{\sqrt{2\pi}\sigma} e^{-\left(\frac{\xi}{\sqrt{2}\sigma}\right)^2} \frac{1}{\gamma\pi} \frac{\gamma^2}{(\lambda - \xi)^2 + \gamma^2} d\xi \\ &= \frac{\gamma}{\sqrt{2}\sigma} \frac{1}{\pi^{3/2}} \int_{-\infty}^{\infty} \frac{e^{-\left(\frac{\xi}{\sqrt{2}\sigma}\right)^2}}{(\lambda - \xi)^2 + \gamma^2} d\xi. \end{aligned} \quad (\text{A.1})$$

We can by making the following substitution, $\xi = \sqrt{2}\sigma t$ and $d\xi = \sqrt{2}\sigma dt$, write it as

$$\begin{aligned} V(\lambda, \sigma, \gamma) &= \frac{\sqrt{2}\sigma}{\sqrt{\pi}} \frac{\gamma}{\pi} \int_{-\infty}^{\infty} \frac{e^{-t^2}}{(\lambda - \sqrt{2}\sigma t)^2 + \gamma^2} dt \\ &= \frac{1}{\sqrt{2\pi}\sigma} \frac{\gamma}{\pi} \int_{-\infty}^{\infty} \frac{e^{-t^2}}{\left(\frac{\lambda}{\sqrt{2}\sigma} - t\right)^2 + \left(\frac{\gamma}{\sqrt{2}\sigma}\right)^2} dt. \end{aligned} \quad (\text{A.2})$$

This form of the convolution is closely related to the complex probability function (Letchworth & Benner 2007; Abrarov & Quine 2015a),

$$W(z) = \frac{i}{\pi} \int_{-\infty}^{\infty} \frac{e^{-t^2}}{z - t} dt \quad (\text{A.3})$$

for any complex argument, $z = x + iy$. The complex probability function can be expressed as a sum of a real and imaginary part (Benner et al. 1995; Abrarov & Quine 2015b),

$$\begin{aligned} W(x, y) &= K(x, y) + iL(x, y) \\ &= \frac{y}{\pi} \int_{-\infty}^{\infty} \frac{e^{-t^2}}{(x - t)^2 + y^2} dt + \frac{i}{\pi} \int_{-\infty}^{\infty} \frac{(x - t)e^{-t^2}}{(x - t)^2 + y^2} dt, \end{aligned} \quad (\text{A.4})$$

where is the real part, $\text{Re}[W(x, y)] = \sqrt{2\pi}\sigma V(\lambda, \sigma, \gamma)$ if $x = \frac{\lambda}{\sqrt{2}\sigma}$ and $y = \frac{\gamma}{\sqrt{2}\sigma}$, which can be obtained by using the complex argument, $z = \frac{\lambda + i\gamma}{\sqrt{2}\sigma}$, in the complex probability function. If $\text{Im}[z] \geq 0$, which is always guaranteed for the width of a spectral profile, the complex probability function equals the complex error function. The complex error function has numerous, fast, numerical approximations where in this work we use the `scipy.special.wofz` (Jones et al. 2001) implementation.

Appendix B: Notes on Individual objects

Appendix B.1: GRB090313 ($z = 3.373$)

Appendix B.2: GRB090530 ($z = 1.266$)

Appendix B.3: GRB090809 ($z = 2.737$)

Appendix B.4: GRB090926 ($z = 2.106$)

Appendix B.5: GRB091018 ($z = 0.971$)

Appendix B.6: GRB091127 ($z = 0.49$)

Appendix B.7: GRB100205A ($z = na$)

Observed 3 days after the *Swift* trigger. No afterglow or host detected in 10.8 ks. GRB likely located at high redshift⁶. The spectrum has not otherwise been published previously.

Appendix B.8: GRB100219A ($z = 4.667$)

The data presented here also formed the basis of GCN # 10441⁷ and is published in Thöne et al. (2013). Observations started 12.5 hours after the *Swift* trigger and has a total exposure time of 4.8 ks. Absorption features, including those of Ly α , from a multitude of ions are detected against the afterglow continuum at $z = 4.667$. Additionally, absorption from an intervening system is found at $z = 2.181$.

Appendix B.9: GRB100316B ($z = 1.180$)

The data presented here also formed the basis of GCN # 10495⁸. The spectrum has not otherwise been published previously. Observations started 44 minutes after the *Swift* trigger and has a total exposure time of 2.4 ks. Absorption features from Fe II, Al II, Al III, Mg II and Mg I are well detected against the afterglow continuum at $z = 1.180$. Additionally, strong absorption lines from Fe II and Mg II from an intervening system are found at $z = 1.063$.

Appendix B.10: GRB100316D ($z = 0.059$)

The data presented here also formed the basis of GCN # 10512⁹, GCN # 10513¹⁰, GCN # 10543¹¹ and is published in Bufano et al. (2012) and Starling et al. (2011). This GRB is very close by and has an associated SN, SN2010bh, and has therefore undergone intense follow-up. The data presented here consists of a subset of the entire VLT/X-shooter campaign, covering the four first observing days while the afterglow still contributes significantly to the total emission. The first observations started 10 hours after the burst, before the SN was discovered, and targeted the star-forming 'A'-region (Starling et al. 2011), not the GRB. A very rich spectrum containing a multitude of emission lines puts the host at $z = 0.059$. For three consecutive nights, 58, 79 and 101 hours after the *Swift* trigger, the afterglow was observed as it transitioned into the spectrum of a high-velocity Ic-BL SN. The observations taken 79 and 101 hours after the burst are taken under programme 084.D-0265(A) (PI: Benetti), but with an identical setup to the first two observations.

⁶ <http://gcn.gsfc.nasa.gov/gcn3/10399.gcn3>

⁷ <http://gcn.gsfc.nasa.gov/gcn3/10441.gcn3>

⁸ <http://gcn.gsfc.nasa.gov/gcn3/10495.gcn3>

⁹ <http://gcn.gsfc.nasa.gov/gcn3/10512.gcn3>

¹⁰ <http://gcn.gsfc.nasa.gov/gcn3/10513.gcn3>

¹¹ <http://gcn.gsfc.nasa.gov/gcn3/10543.gcn3>

Appendix B.11: GRB100418A ($z=0.624$)

The data presented here also formed the basis of GCN # 10620¹² and GCN # 10631¹³ and is published in [De Ugarte Postigo et al. \(2011\)](#). The burst have been followed up in three epochs of observations, 0.4, 1.4, and 2.4 days after the burst, each lasting 4.8 ks. The unambiguous redshift of the host, $z = 0.624$, is found from the simultaneous detection of emission features belonging to nebular lines, including H I, [O II], [O III], [Ne III], [N II], [S II], [S III], and [He I] as well as absorption features due to the presence of Zn II, Cr II, Fe II, Mn II, Mg II, Mg I, Ti II, and Ca II, all at a consistent redshift. Temporal evolution of the fine-structure lines belonging to Fe II* is found between the epochs.

Appendix B.12: GRB100424A ($z=2.465$)

The data presented here also formed the basis of GCN # 14291¹⁴. The spectrum has not otherwise been published previously. Observations carried out, long after the burst has faded. Emission lines from the host are detected at $z = 2.465$.

Appendix B.13: GRB100425A ($z=1.1755$)

The data presented here also formed the basis of GCN # 10684¹⁵ and is used in [Skuladottir \(2010\)](#), but not published elsewhere. Observations started 4 hours after the *Swift* trigger, totaling 2.4 ks. Absorption features from Mg II and Fe II in the afterglow continuum are detected at $z = 1.1755$.

Appendix B.14: GRB100615A ($z=1.398$)

The data presented here also formed the basis of GCN # 14264¹⁶, but not published elsewhere. Host observation of a dark burst ([D'Elia & Stratta 2011](#)) taken long after the afterglow has faded. Emission lines from the host belonging to [O II], [Ne III], [O III] and H α are detected at a common redshift of $z = 1.398$.

Appendix B.15: GRB100621A ($z=0.542$)

The data presented here also formed the basis of GCN # 10876¹⁷, but not published elsewhere. Beginning 7.1 hours after the GRB, 2.4 ks observations reveal emission lines from [O II], H β and [O III] at a common redshift of $z = 0.542$ and a very weak afterglow continuum.

Appendix B.16: GRB100625A ($z=0.452$)

The data presented here is of the candidate host galaxy, taken long after the burst has faded and have not previously been published. 4.8 ks of exposure reveals a weak continuum present in all arms, but an absence of emission lines. This could indicate that the host primarily contains a older stellar population. The redshift, $z = 0.452$, is taken from [Fong et al. \(2013\)](#).

Appendix B.17: GRB100724A* ($z = 1.288$)

The data presented here also formed the basis of GCN # 10971¹⁸. The spectrum has not otherwise been published previously. The observations were carried out in RRM starting 11 min after the GRB trigger. See section 2.2.1, for a description of the RRM scheme. Absorption lines from several ionic species are detected in the afterglow continuum at a common redshift of $z = 1.288$. This is not a part of the statistical sample.

Appendix B.18: GRB100728B ($z=2.106$)

The data presented here also formed the basis of GCN # 11317¹⁹. The spectrum has not otherwise been published previously. Starting 22 hours after the burst trigger, 7.2 ks of observations reveals a faint afterglow continuum with Ly α - and Mg II-absorption at $z = 2.106$. Due to a malfunctioning ADC, the sensitivity of X-shooter is depressed with respect to normal operations, resulting in a poorer throughput. Additionally, the position of the trace on the slit moves due to atmospheric differential refraction.

Appendix B.19: GRB100814A ($z=1.439$)

The spectra presented here has not been published previously. The observations consists of three visits, the first beginning only 0.9 hours after the *Swift* trigger, the other two visits were 2.13 and 98.40 hours after the trigger, respectively. A bright afterglow continuum is present in all visits, allowing identification of absorption features belonging to a wide range of ions at $z = 1.439$. A complex velocity structure in the absorption features belonging to Mg II, shows several components, separated by as much as 500km/s, pointing to a likely merger scenario in the host.

Appendix B.20: GRB100816A ($z=0.805$)

The data presented here also formed the basis of GCN # 11123²⁰. The spectrum has not otherwise been published previously. This short GRB was observed 28.4 hours after the GRB trigger. 4 x 1200 s of exposure reveals two distinct sets of emission lines, spatially offset $\lesssim 1''$, very close in redshift space, $z = 0.8034$ and $z = 0.8049$, indicating either an interacting host or some complex velocity structure of the host. Faint underlying continua are present under both sets of lines.

Appendix B.21: GRB100901A ($z=1.408$)

The data presented here has been published in [Hartoog et al. \(2013\)](#). Because of the unusual lingering brightness of this GRB, 2.4s of observations taken 65.98 hours after the GRB trigger still reveals an afterglow continuum visible across the entire spectral coverage of X-shooter. Absorption lines from a wide range ion put the redshift at $z = 1.408$, with intervening absorption systems at $z = 1.3147$ and $z = 1.3179$.

Appendix B.22: GRB101219A ($z=0.718$)

This data has not been published before. Starting 3.7 hours after the GRB trigger, 7.2 ks of exposure time reveals a very faint continuum in the visual and near-infrared, only visible when heavily

¹² <http://gcn.gsfc.nasa.gov/gcn3/10620.gcn3>

¹³ <http://gcn.gsfc.nasa.gov/gcn3/10631.gcn3>

¹⁴ <http://gcn.gsfc.nasa.gov/gcn3/14291.gcn3>

¹⁵ <http://gcn.gsfc.nasa.gov/gcn3/10684.gcn3>

¹⁶ <http://gcn.gsfc.nasa.gov/gcn3/14264.gcn3>

¹⁷ <http://gcn.gsfc.nasa.gov/gcn3/10876.gcn3>

¹⁸ <http://gcn.gsfc.nasa.gov/gcn3/10971.gcn3>

¹⁹ <http://gcn.gsfc.nasa.gov/gcn3/11317.gcn3>

²⁰ <http://gcn.gsfc.nasa.gov/gcn3/11123.gcn3>

binning the images. No redshift estimate is available from these observations. Late-time Gemini-North observations reveal emission lines from the host at $z = 0.718^{21}$.

Appendix B.23: GRB101219B ($z=0.552$)

The data presented here also formed the basis of GCN # 11579²² and is published in Sparre et al. (2011). The first observation, taken 11.6 hours after the burst trigger and lasting 4.8ks, reveals absorption from Mg II and Mg I in the host located at $z = 0.552$ on a featureless continuum visible across the entire coverage of X-shooter. Subsequent observations taken 16 and 37 days after the trigger shows the fading spectral signature of a SN, SN2010ma.

Appendix B.24: GRB110128A ($z=2.339$)

Appendix B.25: GRB110407A ($z=na$)

Appendix B.26: GRB110709B ($z=na$)

Appendix B.27: GRB110715A ($z=0.82$)

Appendix B.28: GRB110721A ($z=0.382$)

Appendix B.29: GRB110808A ($z=1.348$)

Appendix B.30: GRB110818A ($z=3.36$)

Appendix B.31: GRB111005A ($z=0.013$)

Appendix B.32: GRB111008A ($z=4.989$)

Appendix B.33: GRB111107A ($z=2.893$)

Appendix B.34: GRB111117A ($z=1.3?$)

Appendix B.35: GRB111123A ($z=3.151$)

Appendix B.36: GRB111129A ($z=na$)

Appendix B.37: GRB111209A ($z=0.677$)

Appendix B.38: GRB111211A ($z=0.478$)

Appendix B.39: GRB111228A ($z=0.716$)

Appendix B.40: GRB120118B ($z = 2.943$)

The data presented here also formed the basis of GCN # 14225²³, but is not published otherwise. This late-time observation of the host of GRB120118B consists of 3.6 ks exposures and contains emission lines belonging to [O II] and [O III] at $z = 2.943$, suggested to be redshift of the host.

Appendix B.41: GRB120119A ($z = 1.728$)

The data presented here has not been published before. Three epochs of observations have been obtained, the first two immediately after the burst, and the last one long after the afterglow had faded. Starting 1.4 hours after the *Swift* trigger, the first epoch contains bright afterglow continuum. Rich in absorption features belonging to a multitude of ions, $z = 1.728$ is estimated for the host with intervening systems at $z = 1.476$, $z = 1.214$, $z = 0.662$ and $z = 0.632$. The second epoch, obtained 4.5 hours after the burst contains the fading afterglow. A third epoch is obtained > 1

year after the GRB in which emission lines from H β and H α are found at the redshift of the host, confirming the association of the absorption line system and the host.

Appendix B.42: GRB120211A ($z = 2.346$)

The data presented here has been published in Krühler et al. (2015). Two observations of the host of GRB120211A has been obtained, starting 2013.02.17, > 1 year after the burst has faded. A redshift for this object has been reported by Krühler et al. (2015) and the features seen by those authors are reproduced in these reductions, confirming $z = 2.346$.

Appendix B.43: GRB120224A ($z = 1.10$ NEW!!!)

The data presented here has formed the basis of GCN # 12991²⁴, and has also been published in Krühler et al. (2015). Starting 19.8 hours after the GRB trigger, a total exposure time of 2.4 ks reveals a faint continuum, starting at ~ 700 nm and extending all the way through 2500 nm. We detect a $\sim 2\sigma$ emission line which, if interpreted as H α , gives $z = 1.10$, supporting the redshift reported by Krühler et al. (2015).

Appendix B.44: GRB120311 ($z = 0.350$ NEW!!!)

The data presented here has formed the basis of GCN # 12991²⁵, but is not published otherwise. Starting just before twilight, 3.65 hours after the burst, a faint afterglow continuum is detected at all wavelengths. Due to the faintness of the afterglow, no absorption features are discernible superposed on the continuum. Displaced from the afterglow continuum by $1''.4$, emission lines belonging to H β , [O III] and H α are detected at $z = 0.350$. The line belonging to H α shows some extended emission toward the afterglow continuum. The angular distance between the two sources correspond to a projected distance in the host plane of 6 kpc, posing a potential problem for the host redshift, unless the GRB occurred in a merging system. The extended emission in H α , supports this interpretation. This burst is not apart of the statistical sample.

Appendix B.45: GRB120327A ($z = 2.813$)

The data presented here also formed the basis of GCN # 13134²⁶ and is published in D'Elia et al. (2014). The observation consists of two visits, 2.13 hrs and 29.98 hrs after the burst, with an afterglow continuum visible in all arms for both visits. We detect absorption features from Ly-limit, Ly α , C II/C III*, Si II/Si III*, Al I, Fe II and Mg II are detected at a consistent redshift, $z = 2.813$.

Appendix B.46: GRB120404A ($z = 2.876$)

The data presented here has formed the basis of GCN # 13227²⁷, but is not published otherwise. 9.6 ks integration, starting 15.7 hours after the *Swift*-trigger reveals a low-intensity afterglow continuum on which absorption from Ly α is detected in two distinct regions at redshifts $z = 2.876$ and $z = .255$. These absorption systems are confirmed by ionic absorption features at both of these redshifts.

²¹ <http://gcn.gsfc.nasa.gov/gcn3/11518.gcn3>

²² <http://gcn.gsfc.nasa.gov/gcn3/11579.gcn3>

²³ <http://gcn.gsfc.nasa.gov/gcn3/14225.gcn3>

²⁴ <http://gcn.gsfc.nasa.gov/gcn3/12991.gcn3>

²⁵ <http://gcn.gsfc.nasa.gov/gcn3/12991.gcn3>

²⁶ <http://gcn.gsfc.nasa.gov/gcn3/13134.gcn3>

²⁷ <http://gcn.gsfc.nasa.gov/gcn3/13227.gcn3>

Appendix B.47: GRB120422A ($z = 0.283$)

The data presented here also formed the basis of GCN # 13257²⁸ and is published in Schulze et al. (2014). A GRB-SN, this burst has been followed up multiple times. The data presented here only contain the first epoch in which the afterglow is still visible and before the rise of SN2012bz. Starting 16.5 hours after the burst, 4.8 ks integration time captures both the host and the burst in emission. A blue afterglow continuum is detected at all wavelengths covered by X-shooter, on which Mg II absorption at $z = 0.283$ is found. Offset by $1''.75$, the host is clearly detected at a consistent redshift with a rich emission line spectrum, the lines extending towards to burst.

Appendix B.48: GRB120712A ($z = 4.175$)

The data presented here also formed the basis of GCN # 13460²⁹ and is not published elsewhere. 4.8 ks integration time, starting 10.5 hours after the BAT trigger, shows a bright afterglow continuum starting at ~ 472 nm, signifying the onset of the Lyman alpha forest, for a GRB located at $z = 4.175$. Absorption features from Ly α , Fe II, Mg II and Si II are readily detected at a consistent redshift.

Appendix B.49: GRB120714B ($z = 0.398$)

The data presented here also formed the basis of GCN # 13477³⁰, but is not published elsewhere. Observations of this burst started 7.8 hours after the GRB trigger, lasting 4.8 ks. A continuum is visible across the entire spectral coverage of X-shooter, with both emission lines from [O II], H β , [O III] and H α , as well as absorption from Mg II detected at $z = 0.398$, securely setting it as the redshift of the GRB.

Appendix B.50: GRB120716A ($z = 2.486$)

The data presented here also formed the basis of GCN # 13494³¹, but is not published elsewhere. Despite observations starting 62 hours after the *Swift* trigger and lasting 3.6 ks, a bright afterglow is clearly seen, along with a plethora of absorption features. Absorption of Ly α -photons in the host leaves a broad trough, from which the Lyman alpha forest is visible bluewards, all the way down to the Lyman limit. Metal absorption lines from C II, Si II, [O I], Fe II, C IV, Si IV, including fine structure transitions identified as C II*, Si II*, Fe II* and metastable [Ni II] lines are all detected at $z = 2.486$.

Appendix B.51: GRB120722A ($z = 0.959$)

The data presented here also formed the basis of GCN # 13507³², but is not published elsewhere. On 4.8 ks integration time, starting 10 hours after the burst trigger, the simultaneous detection of absorption features belonging to Mg II and Fe II superposed on a blue continuum, and emission lines from [O II], H γ , H β , [O III] and H α , all at $z = 0.959$, confidently sets it as the redshift of the GRB.

Appendix B.52: GRB120805A ($z \sim 3.9$ NEW!!!)

A separate reduction of this burst has been published in Krühler et al. (2015), but not otherwise. Starting 9 days after the burst trigger, this is host observation and does not contain any afterglow continuum. In 3.6 ks integration time, we detect a faint continuum visible from 450 nm and all the way through 2100 nm, in contrast to what is found previously. The continuum from 4500 - 600 nm is detected at very low significance. If the drop at 450 nm is the Lyman limit, this fits with Lyman alpha at ~ 600 nm, giving $z \sim 3.9$. The absence of nebular lines if due to [O II] falling in a telluric absorption band and the rest being shifted out of the wavelength coverage.

Appendix B.53: GRB120815A* ($z = 2.358$)

Not a part of the statistical sample, this burst also formed the basis of GCN # 13649³³ and is published in Krühler et al. (2013). Observations started 1.69 hours after the BAT trigger and consist of 2.4 ks integration. A bright afterglow continuum is detected across the entire spectral coverage of X-shooter, with a multitude of absorption lines superposed. Absorption features from the host at $z = 2.358$ include a DLA as well as metal absorption lines from [N V], [S II], Si II, [O I], C IV, Si IV, Fe II, Al II, Al III, Mn II, Mg II, and Mg I. Additionally fine-structure lines from [Ni II] and Fe II are exited local to the GRB. Intervening systems are found at $z = 1.539$, $z = 1.693$, and $z = 2.00$.

Appendix B.54: GRB120909A ($z = 3.929$)

The data presented here has formed the basis of GCN # 13730³⁴, but is not published otherwise. A very rapid follow-up, starting only 1.7 hours after the BAT trigger, this 1.2 ks observation captures a very bright afterglow continuum, starting at 450 nm, signifying the onset of the Lyman limit for a system at $z = 3.929$. Absorption from high-column density hydrogen leaves very prominent absorption features in the form of Ly α , Ly β , and Ly γ , visible in the Lyman alpha forest. Metal absorption lines arising from Fe II, [Ni II], Si II, [S II], Al II, Al III, C II, [O I], C IV, and Zn II are all detected along with the corresponding fine-structure lines from (Fe II*, Si II*, [O I]*, [O I]*, C II*), securely anchoring the redshift of the host.

Appendix B.55: GRB120923A ($z \approx 8?$)**Appendix B.56: GRB121024A ($z = 2.300$)**

The data presented here also formed the basis of GCN # 13890³⁵ and is published in Friis et al. (2015). Also rapid, starting 1.8 hours after the *Swift* trigger, a bright afterglow continuum is visible across all arms. A broad absorption feature from Lyman alpha, along with narrow lines from C IV, Si II, Si IV, Fe II, [S II], and Al II, as well as fine-structure lines associated with Si II* are all detected at $z = 2.300$, securely setting it as the redshift of the GRB.

Appendix B.57: GRB121027A ($z = 1.773$)

The data presented here has formed the basis of GCN # 13930³⁶, but is not published otherwise. Starting 69.6 hours after the GRB

²⁸ <http://gcn.gsfc.nasa.gov/gcn3/13257.gcn3>

²⁹ <http://gcn.gsfc.nasa.gov/gcn3/13460.gcn3>

³⁰ <http://gcn.gsfc.nasa.gov/gcn3/13477.gcn3>

³¹ <http://gcn.gsfc.nasa.gov/gcn3/13494.gcn3>

³² <http://gcn.gsfc.nasa.gov/gcn3/13507.gcn3>

³³ <http://gcn.gsfc.nasa.gov/gcn3/13649.gcn3>

³⁴ <http://gcn.gsfc.nasa.gov/gcn3/13730.gcn3>

³⁵ <http://gcn.gsfc.nasa.gov/gcn3/13890.gcn3>

³⁶ <http://gcn.gsfc.nasa.gov/gcn3/13930.gcn3>

trigger, that we detect the afterglow continuum at a so high significance in all arms with 8.4 ks integration, testifies to the brightness of this burst. The concurrent identification of emission lines from [O III] and absorption from C IV, Al II, Al III, Mg I, Mg II, and Fe II, tightly constrains the redshift of the burst to be ($z = 1.773$)

Appendix B.58: GRB121201A ($z = 3.385$)

Appendix B.59: GRB121229A ($z = 2.707$)

Appendix B.60: GRB130131B ($z = 2.539$)

Appendix B.61: GRB130408A ($z = 3.758$)

The data presented here also formed the basis of GCN # 14365³⁷. The spectrum has not otherwise been published previously. The observations consists of two 600sec spectra taken 1.9hrs after the burst. We detect absorption features from a wide range of ions. We also detect intervening absorption at $z = 1.255$ and $z = 3.248$.

Appendix B.62: GRB130418A ($z = 1.218$)

Appendix B.63: GRB130427A ($z = 0.34$)

Appendix B.64: GRB130427B ($z = 2.78$)

Appendix B.65: GRB130603B ($z = 0.356$)

Appendix B.66: GRB130606A ($z = 5.913$)

The data presented here also formed the basis of GCN # 14816³⁸ and is published in Hartoog et al. (2015). The observations consists of three 2x600sec visits starting 7.1 hrs after the burst at fairly high airmass. We detect absorption features from a wide range of ions at $z = 5.913$ as well as intervening absorption at $z = 2.3103, 2.5207, 3.4515, 4.4660, 4.5309, 4.5427, 4.6497$ and 4.7244 .

Appendix B.67: GRB130612A ($z = 2.006$)

Appendix B.68: GRB130615A ($z = 3?$)

Appendix B.69: GRB130701A ($z = 1.155$)

Appendix B.70: GRB131011A ($z = 1.874$)

Appendix B.71: GRB131030A ($z = 1.296$)

Appendix B.72: GRB131103A ($z = 0.599$)

Appendix B.73: GRB131105A ($z = 1.686$)

Appendix B.74: GRB131117A ($z = 4.042$)

Appendix B.75: GRB131231A ($z = 0.642$)

Appendix B.76: GRB140114A ($z = \sim 2.8?$)

Appendix B.77: GRB140213A ($z = 1.208$)

Appendix B.78: GRB140301A ($z = 1.416$)

Appendix B.79: GRB140311A ($z = 4.95$)

Appendix B.80: GRB140430A ($z = 1.601$)

Appendix B.81: GRB140506A ($z = 0.889$)

Appendix B.82: GRB140515A ($z = \sim 6.32?$)

Appendix B.83: GRB140614A ($z = 4.233$)

Appendix B.84: GRB140622A ($z = 0.959$)

Appendix B.85: GRB141028A ($z = 2.332$)

Appendix B.86: GRB141031A ($z = na$)

Appendix B.87: GRB141109A ($z = 2.993$)

Appendix B.88: GRB150206A ($z = 2.087$)

Appendix B.89: GRB150301B ($z = 1.517$)

Appendix B.90: GRB150403A ($z = 2.06$)

Appendix B.91: GRB150423A ($z = 1.394$)

Appendix B.92: GRB150428A ($z = na$)

Appendix B.93: GRB150514A ($z = 0.807$)

Appendix B.94: GRB150518A ($z = 0.256$)

Appendix B.95: GRB150616A ($z = 1.188$)

Appendix B.96: GRB150727A ($z = 0.313$)

Appendix B.97: GRB150821A ($z = 0.755$)

Appendix B.98: GRB150831A ($z = na$)

Appendix B.99: GRB150910A ($z = 1.359$)

Appendix B.100: GRB150915A ($z = 1.968$)

Appendix B.101: GRB151021A ($z = 2.330$)

The data presented here also formed the basis of GCN # 18426³⁹ and is not published elsewhere. The observation was carried out in RRM starting 44 minutes after the GRB trigger. We detect absorption features from a wide range of ions at $z = 2.330$ as well as intervening absorption at $z = 1.49$.

³⁷ <http://gcn.gsfc.nasa.gov/gcn3/14365.gcn3>

³⁸ <http://gcn.gsfc.nasa.gov/gcn3/14816.gcn3>

³⁹ <http://gcn.gsfc.nasa.gov/gcn3/18982.gcn3>

Appendix B.102: GRB151027B ($z = 4.063$)

Appendix B.103: GRB151029A ($z = 1.423$)

Appendix B.104: GRB151031A ($z = 1.167$)

Appendix B.105: GRB160117B ($z = 0.87$)

Appendix B.106: GRB160203A ($z = 3.517$)

The data presented here also formed the basis of GCN # 18982⁴⁰ and is not published elsewhere. The observation was carried out in RRM starting 18 minutes after the GRB trigger. We detect absorption features from a wide range of ions at $z = 3.517$ as well as intervening absorption at $z = 2.203$.

Appendix B.107: GRB160228A ($z = 1.64$)

Appendix B.108: GRB160303A ($z = na$)

Appendix B.109: GRB160314A ($z = 0.726$)

Appendix B.110: GRB160410A ($z = 1.717$)

Appendix B.111: GRB160425A ($z = 0.555$)

Appendix B.112: GRB160625B ($z = 1.406$)

Appendix B.113: GRB160804A ($z = 0.736$)

The data presented here also formed the basis of GCN # 19773⁴¹, but is not published elsewhere. Observations started 22.37 hours after the BAT trigger and lasted for 2.4ks. The afterglow continuum is detected across the entire spectral coverage of X-shooter and absorption lines from Mg I, Mg II, Fe II and Al II are found at $z = 0.736$. At the same redshift, emission lines from [O II], [O III], H α , H β , H γ , [N II], [S II], [S III] are found. A second epoch, lasting 3.6ks, is obtained after the afterglow has faded, confirming the emission line detections.

Appendix B.114: GRB161001A ($z = 0.891?$)

Appendix B.115: GRB161007A ($z = 4.6$??? NEW!!!)

This data has not been published elsewhere. Observations for GRB161007A started 323 hours after the burst trigger and contains the potential host. 4 x 600 seconds of observations reveals a faint continuum rising abruptly above the noise at ~ 685 nm and continuing through 2100 nm. A very low significance continuum is detected at shorter wavelengths, down to ~ 600 nm. If the host is located at $z \sim 4.6$, the drop in continuum flux is the Lyman alpha break and the absence of nebular emission lines is due to [O II] being shifted out of the wavelength coverage. Alternatively, an early-type host at $z = 0.71$ could exhibit the 400 nm break at 600 nm, but due to the preference of long-duration GRBs for star-forming galaxies, this is the least likely explanation, why we believe the high- z solution.

Appendix B.116: GRB161014A ($z = 2.823$)

The data presented here also formed the basis of GCN # 20061⁴², but is not published elsewhere. Starting 11.6 hours after the GRB trigger, 4.8 ks of integration time captures the afterglow continuum across all three spectroscopic arms. A broad absorption

trough due to Lyman alpha is visible, along with metal absorption features from Mg II, Si II, C II, C IV, Al II, Al III, and Fe II, all at $z = 2.823$. Similar to GRB140506 (Fynbo et al. 2014), a break in the continuum shape is detected bluewards of 600 nm, possible signifying some anomalous form of extinction.

Appendix B.117: GRB161023A ($z = 2.710$)

Appendix B.118: GRB161117A ($z = 1.549$)

⁴⁰ <http://gcn.gsfc.nasa.gov/gcn3/18982.gcn3>

⁴¹ <http://gcn.gsfc.nasa.gov/gcn3/19773.gcn3>

⁴² <http://gcn.gsfc.nasa.gov/gcn3/20061.gcn3>